UC San Diego

UC San Diego Electronic Theses and Dissertations

Title

Motor control of heading in foraging versus rearing reveals multiple states for the coordination of head motion with sniffing

Permalink

https://escholarship.org/uc/item/3ds946c2

Author

Liao, Song-Mao

Publication Date

2022

Peer reviewed|Thesis/dissertation

UNIVERSITY OF CALIFORNIA SAN DIEGO

Motor control of heading in foraging versus rearing reveals multiple states for the coordination
of head motion with sniffing

A dissertation submitted in partial satisfaction of the requirements
for the degree Doctor of Philosophy

in

Physics

by

Song-Mao Liao

Committee in charge:

> Professor David Kleinfeld, Chair
> Professor Yoav Freund
> Professor Jill Leutgeb
> Professor Tatyana Sharpee
> Professor Douglas Smith
> Professor Jing Wang

2022

The dissertation of Song-Mao Liao is approved, and it is acceptable in quality and form for publication on microfilm and electronically.

University of California San Diego

2022

DEDICATION

I would like to dedicate this work to my parents, Hsueh-Chien Liao and Ming-Hsueh Li, for their unconditional support, to my wife, Hsuan-Min Ou, for her continuous encouragement, and to myself in 2013, for his courage to start this journey.

TABLE OF CONTENTS

LIST OF FIGURES

LIST OF TABLES

ACKNOWLEDGEMENTS

I would like to thank my advisor, Professor David Kleinfeld, for his generous support and guidance for the past eight years. He trained me to be a researcher. I would like to thank Professor Yoav Freund, Professor Jill Leutgeb, Professor Tatyana Sharpee, Professor Douglas Smith, and Professor Jing Wang for being on my committee. I would like to thank Professor Massimo Vergassola for being on my former committee.

I would like to thank the members of the David Kleinfeld laboratory and the staff in the physics department for helping me when I needed help. I would like to thank Sabrina Tuell, Thomas Spence, Emma Osgood, Nina Zhang, Peyton O'Callaghan, and Zaneta Ku for assisting with my behavioral training. I would like to thank Julia Kuhl for creating illustrations for the laboratory. And thanks to all my friends who made my life in San Diego as a Ph.D. student unforgettable.

Lastly, I would like to thank my family for their love across the Pacific Ocean and my wife, Olivia, for cheering me up by composing lovely and delightful songs.

Chapters 1 through 6 contain parts reformatted from a manuscript in preparation: Liao, S.-M. and Kleinfeld, D., "A change in coordination of orofacial movements induced by the switch between foraging and rearing", 2022. The dissertation author is the primary author of this work.

Chapters 1, 2, and 6 contain parts of the material as it appears in: Kurnikova, A., Moore, J. D., Liao, S.-M., Deschênes, M., and Kleinfeld, D., "Coordination of orofacial motor actions into exploratory behavior by rat", Current Biology, 27(5), 2017. The dissertation author was the co-author of this paper.

VITA

2022   Doctor of Philosophy in Physics, University of California San Diego

2012   Bachelor of Science in Physics, National Taiwan University

ABSTRACT OF THE DISSERTATION

Motor control of heading in foraging versus rearing reveals multiple states for the coordination
of head motion with sniffing

by

Song-Mao Liao

Doctor of Philosophy in Physics

University of California San Diego, 2022

Professor David Kleinfeld, Chair

Breathing, one of the fundamental and indispensable rhythms of life, has been proposed to serve as a "master clock" that binds the orofacial sensory inputs in rodents (Welker, 1964; Kleinfeld et al., 2014). Previous studies showed whisking (Moore et al., 2013; Deschênes et al., 2016), nose twitching (Kurnikova et al., 2017), and head-bobbing (Kurnikova et al., 2017) are one-

to-one phase-locked to breathing as the rat explores its peri-personal space in a head-fixed setting or on a small and confined platform.

In this work, we test this "breathing primacy hypothesis" (Kleinfeld et al., 2014) on the foraging behavior in rats, where the orofacial motor actions may become more complex as the rat has a larger field to explore. First, we delineate the motor control of the horizontal head movement in the allocentric and egocentric coordinates. We show the coordination with breathing is bimodal and depends on the postural states. We record the electromyogram (EMG) from neck muscles and find their activities phase-locked to breathing at distinct phases, suggesting that the breathing rhythm is involved in hierarchical motor control. We explore the dimension along the behavioral repertoire and observe that the phase relationship between the neck muscles and breathing shifts as the rat switches between the foraging and rearing states, accompanied by a change in the sniffing rate. We use models of weakly coupled phase oscillators (Kuramoto, 1984; Kopell and Ermentrout, 1986; Kopell, 1988; Schuster and Wagner, 1989; Ermentrout and Kleinfeld, 2001; Kleinfeld and Mehta, 2006) to explain the experimental results and show that the rat can pattern the motor outputs differently by driving the neck oscillator with different breathing frequencies. Lastly, we delineate the differential coordination of whisking and nose twitching with breathing in the foraging and rearing modes. Together with the insights in the heading control, our work suggests that the fixed connectivity among the brainstem oscillators can generate variable programs of motor outputs to fulfill different behavioral goals.

Chapter 1. Introduction

1.1 Rhythmic orofacial motor actions in rodents

Rodents form naturalistic behaviors with rhythmic orofacial motor actions. In whisking, the macro vibrissae repeatedly protract and retract to scan for tactile information. During chewing and licking, the jaw repeatedly opens and closes to gather life-sustaining nutrients and water. The rhythmicity of these motor plants is proposed to be generated by the oscillators in the brainstem. For example, the whisking oscillator has been identified in the intermediate reticular formation (Moore et al., 2013; Deschênes et al., 2016). Neurons in this region (denoted vIRt) pace the motoneurons of the vibrissa intrinsic protractors by rhythmic inhibition (Deschênes et al., 2016). Putative oscillators for some other orofacial motor actions were also reported to be in the nearby regions in the reticular formation. These motor actions include the twitching of the nose (Kurnikova et al., 2019), chewing (Chandler and Tal, 1986; Nozaki et al., 1986; Nakamura and Katakura, 1995; Stanek IV et al., 2014), and licking (Travers et al., 1997; Travers et al., 2000; Chen et al., 2001; Stanek IV et al., 2014; Dempsey et al., 2021). Each oscillator patterns the outputs of a set of muscles. For example, the chewing oscillator might need to recruit both the lingual muscles (e.g., genioglossus and styloglossus) and the masticatory muscles (e.g., digastric and masseter) to break down the food and to send to swallow. It's crucial that the timing between different muscle groups is paced accurately within each oscillator. Precise coordination is required not only to achieve behavioral goals but also to avoid lethal errors, such as biting the tongue or choking. Moreover, the same motor plant may receive the drives from multiple oscillators. To avoid conflicts, the proper execution of the motor plants relies heavily on a robust coordinating system between different oscillators. Because of the proximity of the putative orofacial oscillators

in the reticular formation, the coordination system is proposed to be located at the level of the brainstem (Moore et al., 2014; Stanek IV et al., 2014).

1.2 Hierarchical orofacial control by breathing

Pioneering studies on the coordination among rhythmic motor outputs were performed by von Holst, who recorded multiple states of "relative coordination" between different fin rays in fish under various conditions (von Holst, 1939/1973). These observations led to the "superimposition hypothesis" that one rhythm process may act upon other rhythmic processes to influence them, or two rhythmic processes may act upon each other to cooperatively alter their amplitudes and frequencies (von Holst, 1939/1973). Can a similar concept of hierarchical interaction be applied to the oscillators for the orofacial motor actions in rodents?

Recently, the breathing oscillator has been proposed to play a critical role in arbitrating orofacial rhythms (Welker, 1964; Moore et al., 2013; Kleinfeld et al., 2014; Moore et al., 2014). The earliest clue came from a report published by Welker in 1964, where he noted that the movements of the head, nose, and vibrissae are correlated with the sniffing cycle (Welker, 1964). Since many orofacial motor plants share the usage of the upper airway, it is reasonable that the breathing rhythm might serve as the arbitrator (Moore et al., 2014). In addition, studies also showed that signal processing in the olfactory system is correlated with breathing in rodents. Neuronal activities in the olfactory bulb in mice (Shusterman et al., 2011; Smear et al., 2011) and the anterior olfactory nucleus pars externa in rats (Kikuta et al., 2010) are in synchrony with respiration, suggesting that the decoding of olfactory information is also paced by the breathing rhythm (Kleinfeld et al., 2014).

Recent work on the whisking circuitry unraveled the hierarchical motor control of vibrissae by breathing (Moore et al., 2013; Moore et al., 2014; Deschênes et al., 2016; McElvain et al., 2018; Takatoh et al., 2022). Until now, three oscillators that generate different phases of the breathing cycle have been identified in the brainstem (Del Negro et al., 2018; Ramirez and Baertsch, 2018): the pre-Bötzinger complex (preBötC) for inspiration (Smith et al., 1991), the postinspiratory complex (PiCo) for post-inspiration (Anderson et al., 2016), and the parafacial area (pF) for active expiration (Pearce et al., 1989; Janczewski and Feldman, 2006; Guyenet et al., 2009; Huckstepp et al., 2015). It has been shown that the preBötC sends projections to reset the whisking oscillator (vIRt) to coordinate vibrissa intrinsic protractors indirectly (Deschênes et al., 2016). The preBötC also directly paces the motoneurons of the extrinsic vibrissa protractors and retractors (Moore et al., 2013; Deschênes et al., 2016). These studies confirmed the role of the breathing rhythm in the hierarchical control of whisking.

Nose-twitching is another example of hierarchical control by breathing. The wiggling of the nose is generated by the activation of the muscle deflector nasi. Unilateral activation of deflector nasi draws the nose ipsilaterally and upward, and balanced bilateral co-activation draws the nose vertically upward (Deschênes et al., 2015; Kurnikova et al., 2017). In head-fixed rats, deflector nasi is activated during expiration and correlated with breathing (Kurnikova et al., 2017). Retrograde tracing from deflector nasi showed labeled cells in the preBötC, supporting the role of the respiratory drive in the hierarchical control (Kurnikova et al., 2019). The preBötC also sends projections to several regions in the brainstem reticular formation that contains the putative feeding oscillators for chewing and licking (Tan et al., 2010). To sum up, all the above evidence supports the "breathing primacy hypothesis" that breathing acts as a reference rhythm to bind multi-modal (e.g., tactile, olfactory, and gustatory) sensory inputs with precise timing during inspiration, and

the orofacial motor plants (e.g., the vibrissae, snout, and tongue) are repositioned to the next peri-personal region during expiration for the subsequent "snapshot" (Uchida and Mainen, 2003; Kleinfeld et al., 2014; Kurnikova et al., 2017).

1.3 Validating breathing primacy hypothesis on foraging head control

Past studies on the coordination of orofacial motor actions and breathing were conducted on head-fixed animals or in a confined apparatus that restricted full locomotion (Moore et al., 2013; Kurnikova et al., 2017). Therefore, it is worthwhile studying animals performing naturalistic behaviors in a larger field and asking if the coordination of the orofacial motor actions with breathing becomes more complex. We choose the foraging behavior to test the breathing primacy hypothesis. Foraging is a complex and dynamic process formed with exploration, navigation, locomotion, head turns, rearing, and rich orofacial motor actions, as the animal searches for life-sustaining nutrients. How does the rat incorporate the orofacial motor plants with breathing to find the food source efficiently? In this work, we also expand the scope and study the coordination of horizontal head movement with breathing during foraging. The horizontal movement of the head is intrinsically different from other motor actions (e.g., whisking, chewing, or licking) because it has a symmetrical axis – the torso midline. It would be interesting to see how the movement relative to the symmetrical axis is programmed and coordinated with breathing in the foraging behavior. Also, the orofacial motor plants (e.g., the vibrissae and nose) not only are driven directly by their musculatures but also are moved indirectly by the head. The movement of the head determines the regions in the peri-personal space where the orofacial motor plants can gather sensory information. By understanding the coordination with the head movements, we can gain

more insights into the underlying circuitries in the brainstem that generate the rhythmic movements of the orofacial motor plants.

In addition to the search on the two-dimensional horizontal surface, rodents in confined (Gharbawie et al., 2004) or open environments (Fonio et al., 2009; Benjamini et al., 2011; Wexler et al., 2018) perform vertical exploratory behaviors. Among the vertical exploratory behaviors, rearing is the typical behavior in rodents in response to novelty or to collect distant cues for spatial information (Lever et al., 2006). The rearing behavior indicates a shifted attention to the vertical dimension in the animal's peri-personal space and should be considered as an intrinsically different behavioral module from the horizontal exploratory repertoire (Gharbawie et al., 2004; Lever et al., 2006). First, rodents in novel environments build up exploratory behaviors with increasing extent and complexity, with vertical exploration developed after horizontal exploration (Fonio et al., 2009; Benjamini et al., 2011; Wexler et al., 2018). Second, rats recovering from akinesia by bilateral hypothalamic damage regain horizontal and vertical movements at different rates (Golani et al., 1979). Third, rearing and horizontal locomotion in rodents can be dissociated by pharmacological manipulations (Hargreaves and Cain, 1992; Wu et al., 2005; Lever et al., 2006). These results motivated us to study the rearing behavior in addition to the horizontal foraging behavior. By delineating the coordination of the head movements with breathing in the foraging and rearing behaviors, we can understand how the rat incorporates its orofacial motor plants, which are hard-wired in the sensorimotor system, into diverse behaviors in natural environments.

Chapter 2 describes the details of the experimental procedures and the pipeline of data processing. In Chapter 3, we study how the heading control coordinates with breathing in rats undertaking foraging and rearing modes. In Chapter 4, we report our results of electromyogram (EMG) recordings from the neck muscles and delineate their coordination with breathing and the

synergistic outputs. We use weakly coupled oscillators (Kuramoto, 1984; Kopell and Ermentrout, 1986; Kopell, 1988; Delaney et al., 1994; Roelfsema et al., 1997; Golubitsky et al., 1998; Ermentrout and Kleinfeld, 2001; Buchli and Ijspeert, 2004; Ghigliazza and Holmes, 2004; Kleinfeld and Mehta, 2006) to model the interaction between breathing and head movement and discuss how motor outputs can be reprogrammed to form different behaviors with fixed connections in the brainstem circuitry. In Chapter 5, we revisit whisking and nose-wiggling and delineate their new features in the foraging and rearing states. Lastly, Chapter 6 summarizes the results.

Acknowledgements

Chapter 2. Materials and methods

Behavioral training and surgical procedures were in accordance with the animal use protocol approved by the Institutional Animal Care and Use Committee (IACUC) at the University of California San Diego.

2.1 Experimental subjects

Thirty-three Long-Evans adult female rats, with body weights ranging from 240 grams to 430 grams, were used in this study.

2.2 Behavioral training

Animals (Long-Evans rats) were trained to forage for food under food restrictions. Before food restriction, body weight was measured as the baseline. Each food restriction period was no longer than five consecutive days. After five consecutive days of food restriction, animals had at least two days of ad libitum food access.

Animals were weighed daily during the food restriction period. The current food restriction period ended immediately if the weight dropped below $0.8 \times$ baseline. During the food restriction period, supplemental food was provided to ensure that the rats were not deprived of food for more than 24 hours.

During the training and recording sessions, the rat was placed inside the foraging arena. Food pellets were dropped into the arena one at a time at random locations after an auditory cue. The experiment ended when the rat no longer foraged for food.

2.3 Surgical procedures

All surgical procedures were in accordance with the animal use protocol approved by the Institutional Animal Care and Use Committee (IACUC) at the University of California San Diego.

Surgeries were performed under the injection of ketamine (50 mg/kg-rat) and xylazine (5 mg/kg-rat). The level of anesthesia was monitored regularly by pinching the foot pad. Supplemental doses of ketamine (15 mg/kg-rat) and xylazine (1.5 mg/kg-rat) were provided when needed. Injection of buprenorphine (0.03-0.05 mg/kg-rat) was given before and after the surgery. At surgery, an incision was made along the midline above the skull to the nose. After cleaning the skull surface, 6-8 head screws (McMaster-Carr) were implanted. A hole (Bur Carbide FG ½, Henry Schein) was drilled on top of the nasal cavity, and a sterile thermocouple (5TC-TT-K-36-36, Omega) was inserted into the nasal cavity. The thermocouple wires were attached to the skull with Loctite 401 and Jet Acrylic (Lang Dental), and the end was soldered to a pair of 2.5 mm male pins connectors.

The electromyogram (EMG) electrodes were made with tungsten wires (#795500, A-M Systems). A pair of tungsten wires (coating removed at ~1 mm at the tips) were aligned with a 1-3 mm distance between the bare tips, depending on the size of the target muscle. The tips of the electrodes were bent to create a hook. For EMG recordings in intrinsic vibrissae muscles, bipolar needle electrodes (Loeb and Gans, 1986) were used, where the electrodes are passed through a 25-26G hypodermic needle. For EMG recordings in all other muscles, bipolar suture electrodes (Loeb and Gans, 1986) were used, where the hook of the tungsten electrodes is tied to a silk suture. Electrodes were autoclaved before surgery. For implanting electrodes to the vibrissa intrinsic muscles, the hypodermic needle was passed subcutaneously from above the nasal bone to reach the vibrissae follicles. The needle was then gently pulled out, leaving the electrodes in place. For

implanting electrodes into all other muscles, surgical procedures were performed to expose the target muscle. Target muscles were identified using literature as references (Bekele, 1983; Brichta et al., 1987; Callister et al., 1987; Hill et al., 2008; Deschênes et al., 2015) and dissection studies (15 animals). Muscles deflector nasi and nasolabialis were accessed from above the nasal bone. Access from the dorsal neck was made to expose muscles splenius, biventer cervicis, and clavotrapezius. Access from the ventral neck was made to expose muscles sternomastoid and cleidomastoid. After exposing the target muscle, a silk suture was passed through the muscle belly gently to drag the electrodes into the muscle body. After exiting, the silk was tied back to the facia near the entry point to secure the location of the electrodes. We used electrical stimulation (Model 2100, A-M Systems) to re-confirm the location of the implanted electrodes by sending a pulse train of 0.2 milliseconds duration, 4.8 milliseconds burst width, 1.2 milliseconds inter-pulse period, and 100-500 µA of current (Hill et al., 2008). A reference electrode was made with a tungsten wire (#795500, A-M Systems), with ~5 mm striped from the tip. The reference electrode was placed under the skin near the incision. The ground wire was made of a silver wire (#786000, A-M Systems) soldered to one of the head screws. Finally, the ends of the tungsten and silver electrodes were soldered to 10-pin male connectors (Samtec). All surgical incisions were closed with sutures.

In 17 animals, an orientation sensor was implanted into the torso subcutaneously between T1-T6 vertebrae by incision on the back. The torso sensor (BNO055, Adafruit) was covered with epoxy for insulation and sterilized. The surgical incision was closed with sutures. In all animals, a 10-pin female connector (Samtec) was fixed to the skull with Jet Acrylic. The head orientation sensor (BNO055, Adafruit) was attached to the connector before the start of each recording session. After surgery, animals took rest for at least two full days. Post-operative animals were

checked regularly to monitor their conditions. Details of the procedures of each animal reported in

this work are listed in Table 1.

Table 1: Surgical procedures in this work. In all animals, a thermocouple is implanted, and a head sensor is attached. L: Left muscle. R: Right muscle. SM: Sternomastoid. CM: Cleidomastoid. CT: Clavotrapezius. SP: Splenius. BC: Biventer cervicis. VI: Vibrissa intrinsic. NL: Nasolabialis. DN: Deflector nasi. Torso: Torso sensor.

#	ID	SM	CM	CT	SP	BC	VI	NL	DN	Torso
1	SLR087									X
2	SLR089									X
3	SLR090									X
4	SLR092									X
5	SLR093									X
6	SLR094				L + R					
7	SLR095									X
8	SLR096			L + R	L + R					
9	SLR097			L + R	L + R					
10	SLR099						L	L + R	R	
11	SLR100								L + R	
12	SLR102			L + R						X
13	SLR103			L + R						X
14	SLR105			L + R						X
15	SLR106			L + R						X
16	SLR107		L + R							
17	SLR108		L + R							X
18	SLR110	L + R	L + R							X
19	SLR111	L + R	L + R							X
20	SLR112				L + R	L + R				X
21	SLR113				L + R	L + R				X
22	SLR114	L + R								
23	SLR115				L + R	L + R				X
24	SLR116						L + R		L + R	
25	SLR117						L + R		L + R	
26	SLR119	L	L	L	L					X
27	SLR120			L	L	L			L	
28	SLR121			L	L	L			L	
29	SLR122	L	L	L					L	
30	SLR123	L	L	L		L				
31	SLR124	L	L		L	L				
32	SLR125						L + R	L + R		
33	SLR126						L + R	L + R		

2.4 Video annotation and location tracking

As the rat was foraging inside the arena, the entire foraging process was recorded by a Basler camera (acA2040-90umNIR) above the arena at 20 fps. We used DeepLabCut (Mathis et al., 2018; Nath et al., 2019), a 2-D convolutional neural network-based algorithm, to track the animal's location. From each recording video, about 20 frames picked by DeepLabCut were labeled manually to mark the location of the rat's lower (sacral) torso. The labeled data were split into a 19:1 ratio for training and validation. We used a batch size of 1 and a learning rate of 0.005 with the SGD optimizer and trained a Resnet-50 model (Insafutdinov et al., 2016; He et al., 2016) for two iterations (20,000 epochs each). Other parameters were set to default. The tracking results were saved as a CSV file. To locate the center of the arena, we fitted the floor boundary with an ellipse (Gal, 2022).

We inspected all video files to manually label the frames where the rat performed miscellaneous behaviors, including scratching, dog-shaking, grooming, urinating, defecating, biting, and freezing. Data taken under these miscellaneous behaviors were not used in the analyses.

2.5 Data recording and pre-processing

The breathing signal was recorded from the rat by connecting the thermocouple to an amplifier (DAM80, World Precision Instruments). We used a 0.1 Hz high-pass filter, 100 Hz low-pass filter, and ×10000 gain. The connectors of the EMG electrodes were connected to a homemade pre-amplification stage to obtain a gain of ×400 and were high passed at 0.1 Hz (https://neurophysics.ucsd.edu/lab/16_channel_ephys_second_stage.pdf). Breathing and EMG signals were recorded at 20 kHz (40 kHz in six animals) with the data acquisition system (PowerLab, ADInstruments) and were saved to the hard drive.

Head and torso orientation sensors (BNO055, Adafruit) were connected to a development board (Teensy 3.2, PJRC) via the I2C port. The orientation and movement signals from the head and torso sensors were read by Arduino code adopted from the Adafruit BNO055 library (https://github.com/adafruit/Adafruit_BNO055). Signals were sampled at 100 Hz, and the timestamps of each sample were sent to the breathing and EMG acquisition system with a pulse signal. Sensor data were displayed on the Arduino Serial Monitor and were saved to the hard drive at the end of each recording session.

Pre-processing of data was done in MATLAB (MathWorks) code. First, we took the difference in the EMG signals between the electrode pair to obtain the differential EMG. The differential EMG was low passed at 300 Hz by a third order Butterworth low-pass filter and high passed at 9,999 Hz by a third order Butterworth high-pass filter. We then obtained the demodulated EMG envelope by taking the absolute value of the signal, low passed at 50 Hz with a third-order Butterworth filter, and down-sampled it to 2 kHz.

Digitized breathing data were low passed at 20 Hz with a fifth-order Butterworth filter, high passed at 1 Hz with a third-order Butterworth filter, and down-sampled to 2 kHz.

The torso location-tracking data (see Chapter 2.4) were low passed at 4 Hz with a third-order Butterworth filter and were interpolated to 2 kHz with a cubic spline.

The head and torso orientation data were interpolated to 20 kHz with a cubic spline. The head orientation data were low passed at 25 Hz with a third-order Butterworth filter. The torso orientation data were low passed at 4 Hz with a third-order Butterworth filter. Finally, we took the difference between the head yaw and torso yaw to obtain the relative head-torso yaw, and we set the mean of the head-torso yaw angle of the entire recording to zero.

All digital filters were run in both forward and reverse directions to zero phase distortion.

2.6 Data analysis

Data analysis was performed with MATLAB (MathWorks) code. Spectral analyses (spectra and coherence) were performed with the MATLAB Chronux package (Mitra and Bokil, 2008; Kleinfeld and Mitra, 2014; http://chronux.org/). The processing of the breathing signal followed the standard routines in a previous study (Kurnikova et al., 2017). We applied the Hilbert transform to locate the breathing signal's local peaks (corresponding to maximal inhalation) and local troughs (corresponding to maximal exhalation). The inspiration onsets were defined to be the 10% rise times from every trough to its following peak.

To extract the peaks from the pre-processed EMG envelope (Chapter 2.5), we used the 90th percentile value (calculated from all recording sessions in the same animal) as the minimum height threshold. We used 0.5×standard deviation (calculated from all recording sessions in the same animal) as the minimum prominence. We removed outliers whose values are greater than the 99.99^{th} percentile. To extract the peaks in the movement signals from head and torso sensors, we used the 75th percentile value as the minimum height and 0.5×standard deviation as the minimum prominence.

Acknowledgements

behavior by rat", Current Biology, 27(5), 2017. The dissertation author was the co-author of this paper.

3.1 Foraging and rearing inside the arena

We train rats to forage inside an arena of one-meter diameter (Figure 1A). After an auditory cue, food pellets are dropped into random locations in the arena one at a time. The foraging session is run in the dark to reduce the utilization of visual information. The rat's location is tracked with DeepLabCut (Mathis et al., 2018; Nath et al., 2019). The trajectories show that the rat takes curvilinear paths visiting multiple locations in the arena (Figure 1B).
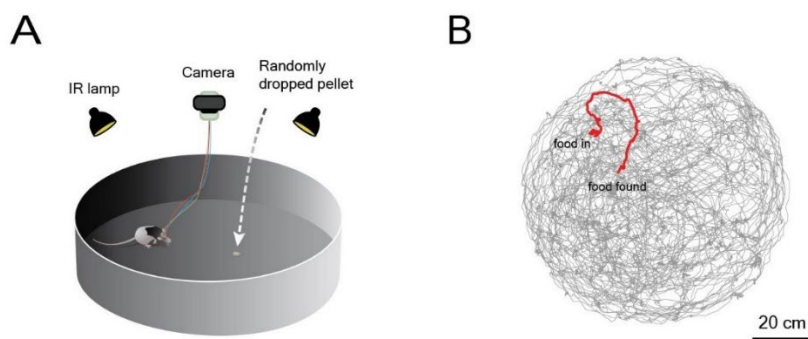
Figure 1: (A) Rat forages inside an arena (diameter = 1 m) for food pellets (B) Trajectories of 72 foraging trials by one rat. The red trajectory shows the path of a single foraging trial in Figure 5.

We measure the breathing signal in 33 rats by implanting a thermocouple (5TC-TT-K-36-36, Omega) into the nasal cavity (Figure 2). We flip the polarity of the thermocouple so that increasing voltage values indicate inhaling and decreasing voltage values indicate exhaling. We simultaneously measure the movements of the head by attaching an orientation sensor (BNO055, Adafruit) to the skull (Figure 2). The orientation sensor provides the head's orientation, angular velocities, and accelerations in the three-dimensional space. In 17 rats, a second orientation sensor is embedded subcutaneously in the torso to measure the torso's orientation, angular velocities, and

accelerations (Figure 2). In both the measurements of head and torso movements, we define the horizontal (yaw) rotation to be positive when the turning is clockwise (CW, viewed from above) and negative when the turning is counterclockwise (CCW). Likewise, we define the vertical (pitch) rotation to be positive when the turning is upward against gravity (Up) and negative when the turning is downward (Down).
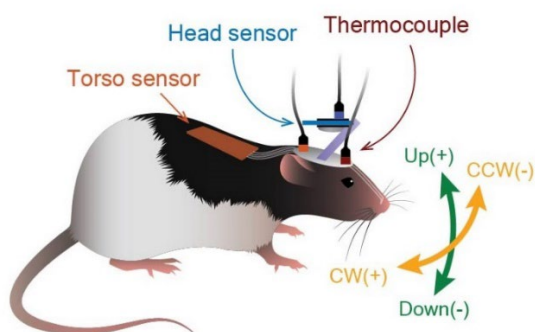
Figure 2: Recording of breathing and head/torso movements with the definitions of signs.

We manually inspect the video data and remove frames where the rat performs miscellaneous behaviors such as scratching and grooming (see Chapter 2.4). When examining the videos of the recording sessions, we note that as the rat is foraging, it places its head near the floor and performs rich head movements and locomotion to visit multiple locations in the arena (Figure 1B). We denote this dominating behavioral mode as the "foraging" state (Figure 3A). In addition to the foraging state, the rat occasionally stops its locomotion and rears up to sniff in the air. We denote this behavioral mode as the "rearing" state (Figure 3A). The foraging and rearing states reflect different behavioral contexts and underlying proposes (Chapter 1.3). To categorize these two states quantitively, we use the pitch angle of the head as the sole feature. Figure 3B shows the probability density distribution of the head pitch angle from 29 rats. We fit the distribution with

three Gaussians and use the intersections (-16.5° and 43.5°) as the thresholds for defining the behavioral states. The animal is defined to be in the foraging state if its head pitch is below -16.5° and in the rearing state if its head pitch is above 43.5° (Figure 3B). We don't use the data where the head pitch is lying between -16.5° and 43.5° or when the rat is performing miscellaneous behaviors (see Chapter 2.4). We keep these threshold values (-16.5° and 43.5°) as our hyperparameters for later analysis of new animals.
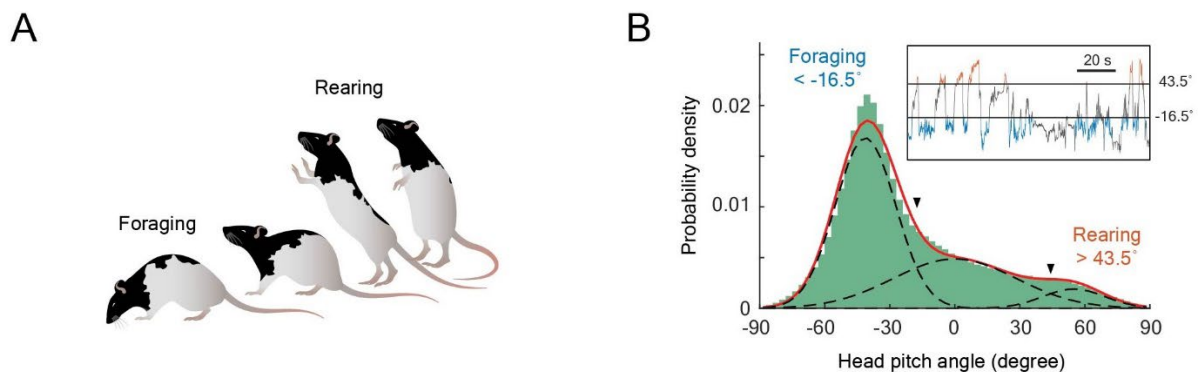
Figure 3: (A) Illustration of the foraging and rearing states. (B) Probability density distribution of head pitch angle fitted with three Gaussians. Data pooled from 29 rats. Inlet shows a recording epoch with behavioral classification (blue: foraging, red: rearing).

With this behavioral classification scheme, the whole recording session can be visualized as a time series interleaved with different behavioral modes, as the animal switches between foraging and rearing states (Figure 4). We will compare the coordination of orofacial motor actions with breathing in these two states.
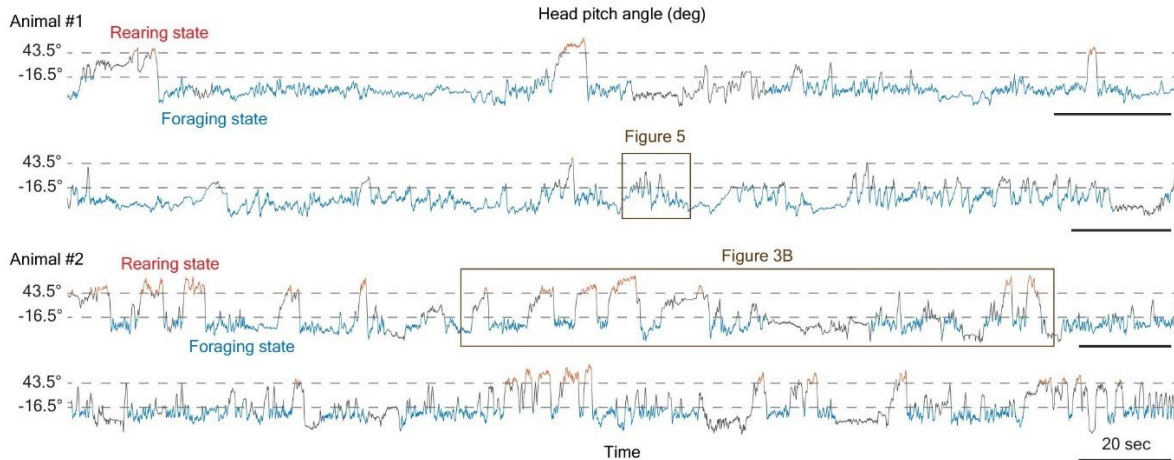
Figure 4: Classification of the foraging (blue) and rearing (red) states. Data from four recording sessions of two rats.

3.2 Rhythmic head movements and breathing

We start by delineating the control of the head movement in the foraging state. Figure 5 shows the example data of a foraging epoch. We define the relative head-torso yaw by subtracting the torso yaw angle from the head yaw angle and removing the offset associated with that recording session (see Chapter 2.5). The dynamics of the head-torso yaw angle reflects the motor control strategy of the heading in the rat's egocentric coordinate, i.e., with the torso midline as the reference. The probability density distribution of the head-torso yaw angle is shown in Figure 6, ranging from -60° to +60° (n = 17).
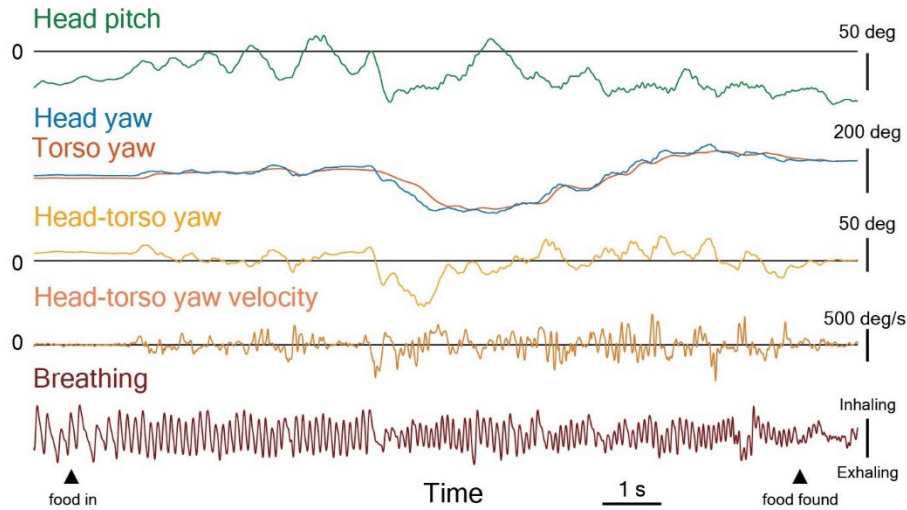
Figure 5: Example data of head/torso movements and breathing in a foraging epoch.
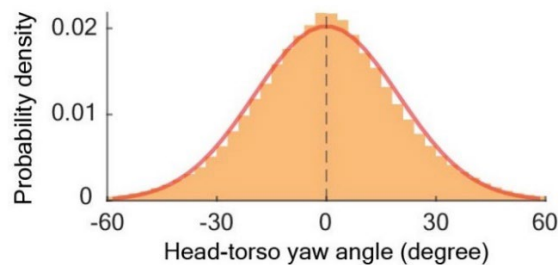
Figure 6: Probability density distribution of the head-torso yaw angle. Data pooled from 17 animals. The red curve shows the Gaussian fit (mean = 0°, std = 19.7°).

In all rats, breathing is recorded simultaneously (n = 33, Figure 5). Based on the frequency (reciprocal of the period), breathing cycles in rodents can be categorized into "basal breathing" (less than 4 Hz) or "sniffing" (more than 4 Hz; Kepecs et al., 2007; Moore et al., 2013). During foraging, the breathing rhythm is dominated by sniffing ranging from 8 Hz to 14 Hz (Figure 7; Figure 8). This frequency band is faster than the sniffing rate recorded from head-fixed animals (4 Hz to 8 Hz; Moore et al., 2013; Kurnikova et al., 2017). We also find that as the animal switches from foraging to rearing, the sniffing rate drops to a slower range of 6-10 Hz (Figure 9). The

phenomenon is observed in 32 of 33 rats (P < 0.001 in 32 of 33 rats, Kolmogorov-Smirnov test). Interestingly, these two different ranges of sniffing rates (during rearing and foraging) were also observed by Kepecs et al. in freely moving rats during odor sampling (6 – 9 Hz) and the pre-reward periods (9 – 12 Hz; Kepecs et al., 2007). In that report, Kepecs et al. discussed the two different sniffing modes in the aspects of "information sampling" and "reward prediction" (Kepecs et al., 2007). We will discuss another possible reason for this frequency shift in Chapter 4 and Chapter 5 as we use computational models to study the motor control of the head and the nose.

We find that horizontal head movement is the superposition of two rhythms in the foraging state. It consists of a slower rhythm lower than 5 Hz and a faster rhythm centered at around 10 Hz (Figure 7; Figure 8). We denote the slower component as "head orientation", where the animal is taking a longer turn to reposition its head into a different mean direction. We denote the faster component as "head scanning", where the animal is making wiggles of small magnitudes for a confined and localized search. The two components correspond to different functional goals. It is reminiscent of the vibrissae movement in which the motion of the vibrissae is the superposition of a faster whisking component and a slow-varying component of the set-points (Berg and Kleinfeld, 2003; Hill et al., 2008; McElvain et al., 2018).

We find the movement of the head is correlated with breathing (Figure 10). The coherence analysis between the head-torso yaw velocity and breathing shows that the two rhythms are phase-locked (Figure 8B). Head-scanning is phase-locked with sniffing in all rats (above the 95% confidence interval, n = 17), and head orientation is phase-locked with basal breathing in 7 of 17 rats. The result confirms that, like whisking (Moore et al., 2013) and nose twitching (Kurnikova et al., 2017), horizontal head movement (head scanning and orientation) shares the same drive with respiration (sniffing and basal breathing).
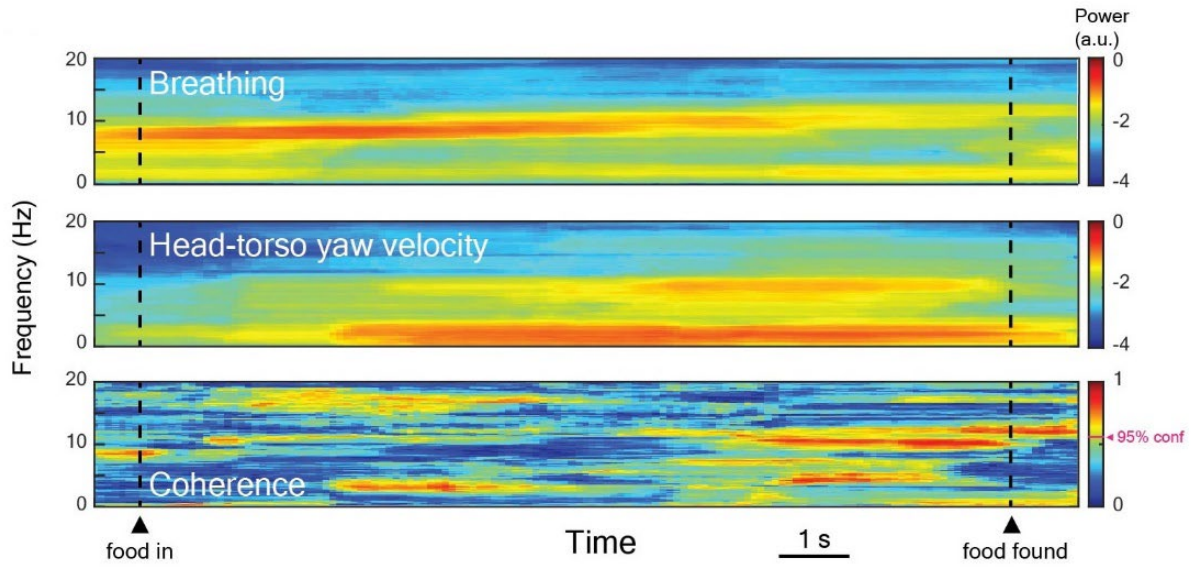
Figure 7: Spectrograms of breathing, head-torso yaw velocity, and their coherence during a foraging trial (data shown in Figure 5). Spectrograms and coherence were calculated with a moving window of size 5 seconds and step size of 0.1 seconds. Half-bandwidth = 1 Hz, with 9 tapers. 95% confidence level of coherence: 0.56.
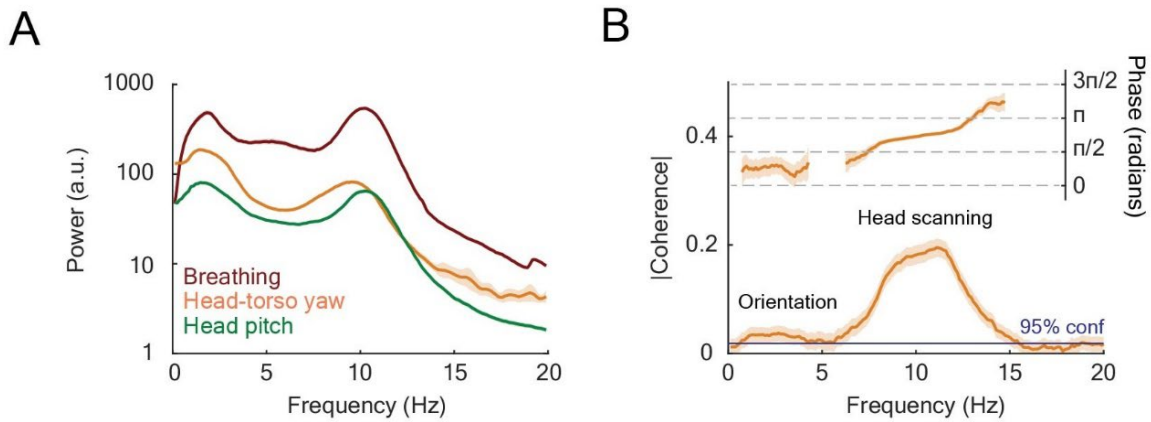
Figure 8: **(A)** Spectra of breathing and the velocities of head-torso yaw and head pitch. Data are shown with Jackknife error bars. Data from one animal (582 windows of size = 4 s, half-bandwidth = 1 Hz, with 7 tapers). **(B)** Coherence between breathing and head-torso yaw velocity during foraging. Data from one animal (582 windows of size 4 seconds, half-bandwidth = 2 Hz, 15 tapers). The horizontal line indicates the 95% confidence level.

21
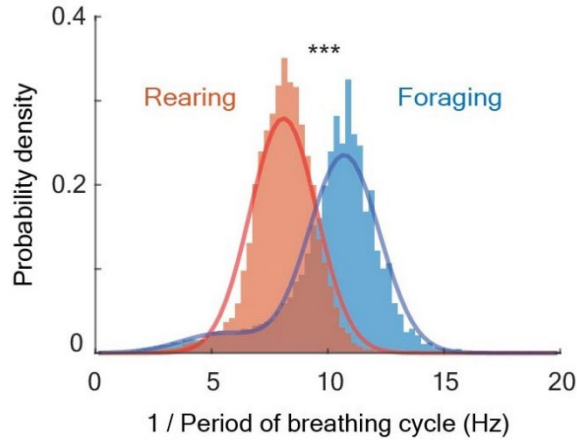
Figure 9: Probability density distributions of the sniffing rate in the foraging and rearing states (P < 0.001, Kolmogorov-Smirnov test). Data from 33 animals. The red curve shows the Gaussian fit (mean: 8.1 Hz, std: 1.4 Hz) to the rearing state. The blue curve shows the fit with two Gaussians (first Gaussian: coefficient = 0.10, mean = 5.5 Hz, std = 1.8 Hz; second Gaussian: coefficient = 0.90, mean = 10.7 Hz, std = 1.5 Hz) to the foraging state.
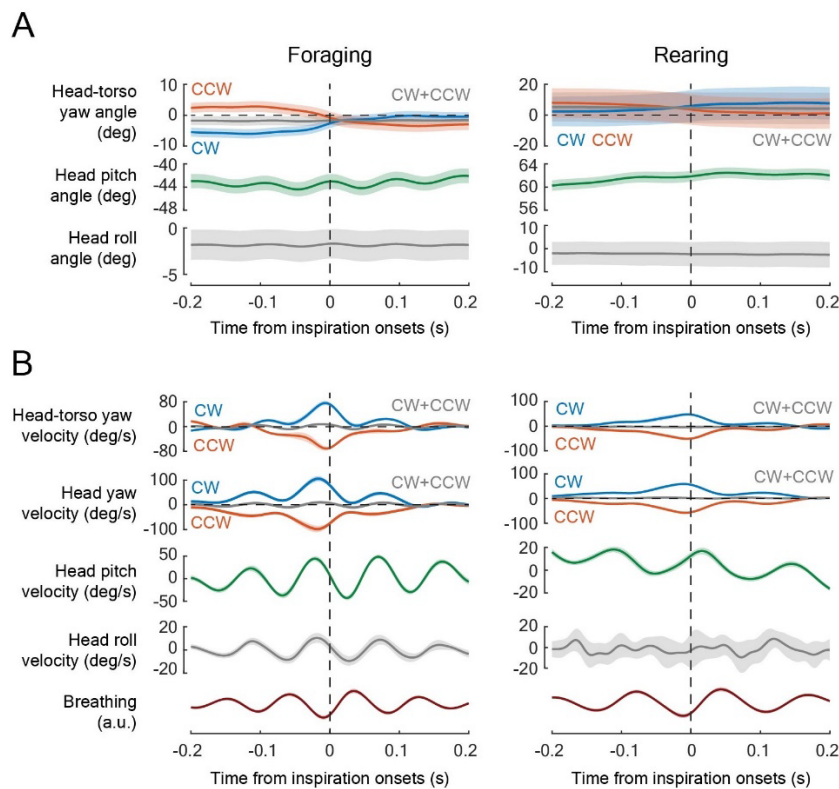
Figure 10: Average (A) angle and (B) velocity of the head with respect to inspiration onsets during foraging and rearing. Error bars are standard errors across animals. Data of head-torso yaw data pooled from 17/15 animals in the foraging/rearing states. Pitch and roll data pooled from 33/31 animals (two do not have rearing epochs longer than 0.4 seconds).

3.3 Bimodal patterns in head scanning

The coherence analysis only reports the power that is linearly transferred between the two signals. To identify any nonlinear patterns, we extract all the peaks (clockwise head scans) and troughs (counterclockwise head scans) of the head-torso yaw velocity data (Figure 11) and make the raster plot of the peaks with respect to the inspiration onsets (Figure 12). In both directions (CW and CCW), we observe two clusters of the peaks inside the sniff cycle – one cluster during inspiration and the other during expiration (Figure 12; Figure 13). We call them inspiratory (INS) and expiratory (EXP) head scans, respectively.
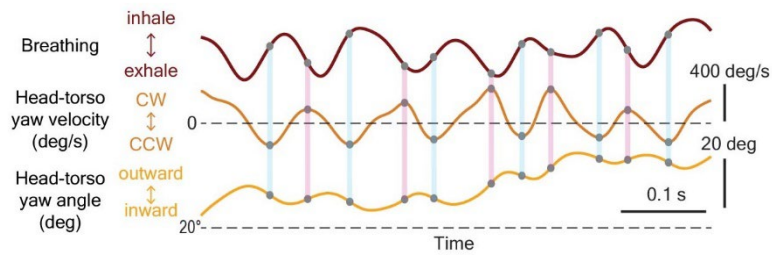
Figure 11: Identification of the clockwise and counterclockwise peaks (grey dots) in head scanning.
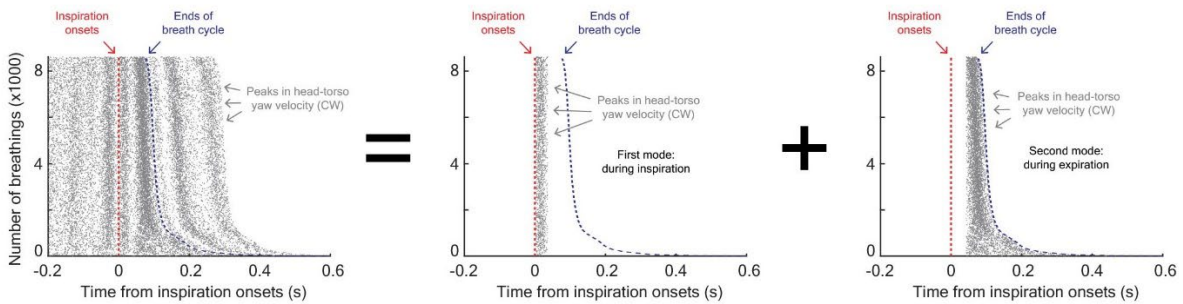
Figure 12: Raster plots of clockwise (left) head scanning peaks with respect to inspiration onsets. Illustrations of the inspiratory (middle) and expiratory (right) modes are shown separately. Breathing cycles are sorted vertically by lengths. Data from one animal.
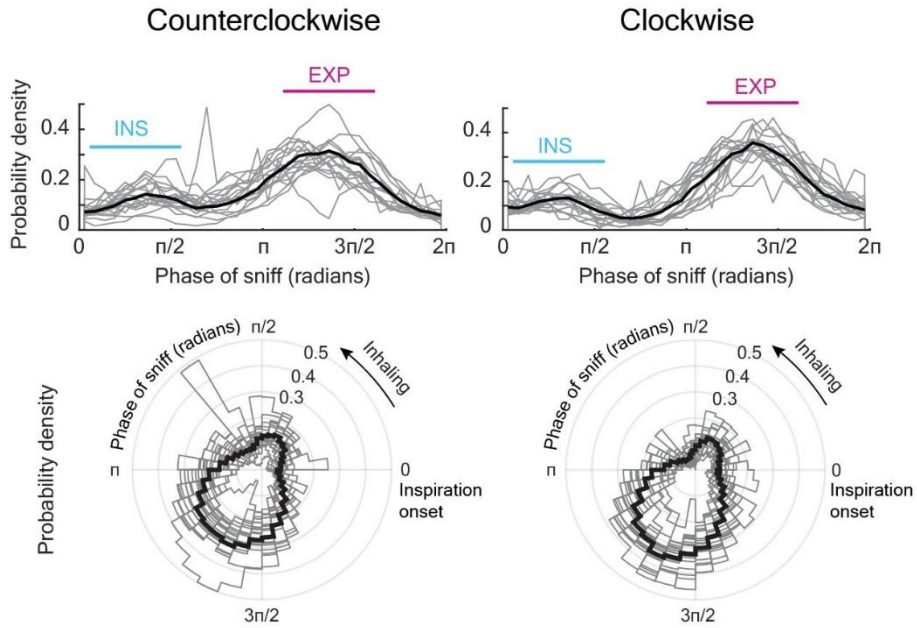
Figure 13: **(Top)** Probability density of inspiratory (INS) and expiratory (EXP) head scans in the sniff cycle. **(Bottom)** Polar histograms of the probability density of INS and EXP head scans. Counterclockwise (left) and clockwise (right) scans are plotted separately. Data from 17 animals. The black curve shows the mean of 17 animals.

The bimodal (inspiratory and expiratory) pattern of correlation between head scanning and sniffing is novel compared to other orofacial behaviors (e.g., nose-wiggling and head-bobbing) that only take upon a single preferred phase inside a sniff (Kurnikova et al., 2017). To better understand their intrinsic properties statistically, we select the head scans that reach the maximal speed within a window of size $\pi/2$ radians centered at 0.96 radians (55 degrees) and 4.28 radians (245 degrees) in the sniff (8-14 Hz) cycle to represent inspiratory and expiratory head scans respectively. We ask what behavioral contexts or features can distinguish inspiratory and expiratory head scans. In 17 rats with an implanted torso tensor, we plot the probability density distributions of the animal's distance to the arena wall and the speed of locomotion of inspiratory and expiratory head scanning (Figure 14). For the distance to the wall, we observe 6 rats have $P < 0.05$ between the two modes (Figure 14B, Kolmogorov–Smirnov test). In the other 11 rats, we are

24

unable to reject the null hypothesis that the two samples are from the same probability distribution. The speed of locomotion in 11 rats is a feature to tell apart inspiratory and expiratory head scans (Figure 14C, P < 0.001 in 11 of 17 animals, Kolmogorov–Smirnov test).
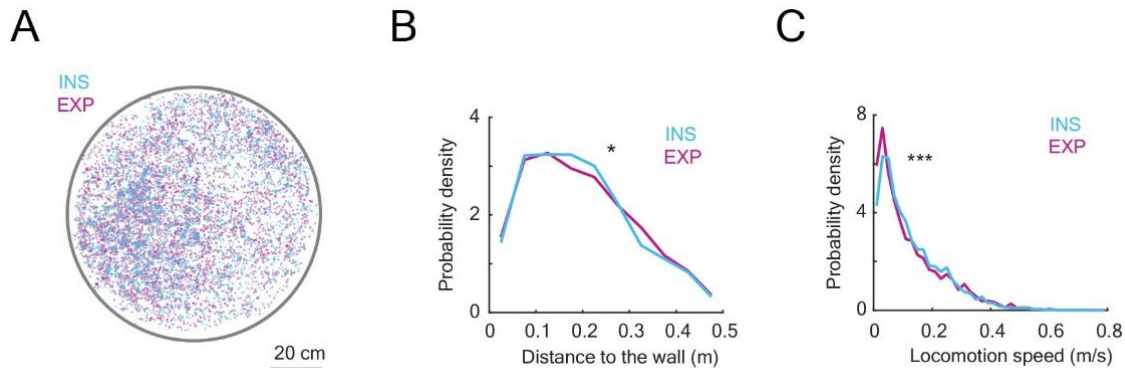
Figure 14: (A) Locations in the arena where the rat makes inspiratory (INS) or expiratory (EXP) head scans. (B) Probability density distributions of INS and EXP head scans as a function of the distance to the wall. (C) Probability density distributions of INS and EXP head scans as a function of the locomotion speed. Data from one animal.

In all rats, we find the probability distribution of the instantaneous head-torso yaw velocity is significantly different between inspiratory and expiratory head scans (Figure 15). We plot the distribution of clockwise and counterclockwise head scans separately. In both directions, we have P < 0.001 in 16 of 17 rats (Kolmogorov–Smirnov test). The one remaining animal has P < 0.05. We find that the distribution of expiratory head scanning has a larger tail than the distribution of inspiratory head scanning. It suggests that, in general, the speed of the head is faster in expiratory head scans and slower in inspiratory head scans (in the rat's egocentric coordinates). This is consistent with the notion of the "breathing primacy hypothesis" (Chapter 1.2) that the rat might use the inspiration to gather a batch of sensory information (Kleinfeld et al., 2014; Kurnikova et al., 2017). Therefore, it is beneficial to the animal to minimize the speed of the head so that it

obtains the greatest spatial resolution to decode sensory information. On the other hand, the exhalation phase is supposed to be the time window for the animal to reposition its orofacial motor plants into the next neighboring location for the subsequent sniff (Kurnikova et al., 2017). Therefore, in general, the speed of the head is faster during the expiratory head scanning. Our data support the breathing primacy hypothesis.
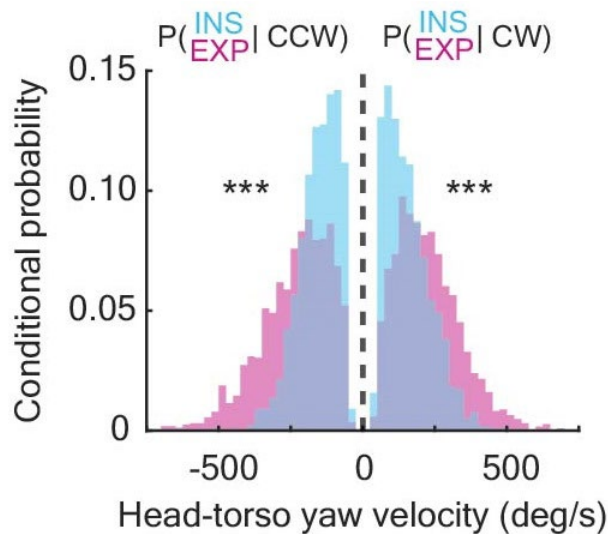
Figure 15: Probability distributions of the head-torso yaw velocity of INS and EXP head scans, conditioned on the direction (CW or CCW) of the scan. Data from one animal.

Figure 16 shows the probability density distributions of INS and EXP head scans as a function of the instantaneous head-torso yaw angle. It shows that regardless of the direction (CW or CCW) of the scan, head scanning is more likely to be inspiratory when the head is turning inward to the torso midline and is more likely to be expiratory when the head is turning outward away from the torso midline (P < 0.001 in 16 of 17 animals). This "inward-inspiratory/outward-expiratory" coordination is also observed in mice (Findley et al., 2021). We hypothesize that as the rat forages, the region that is further away from it is more likely to be the unvisited area where

the rat has less information. As a result, scanning away from the torso midline is more likely to be bound to the expiratory phase as the rat relocates to the next area of interest for subsequent information sampling (Figure 17). By comparison, this bimodal division is less evident when the rat is in the rearing state (Figure 18).

To sum up, by recording the movements of the head and torso directly from wearable sensors, we show that the horizontal head movement is coordinated with breathing in a bimodal (inspiratory inward and expiratory outward) way that supports the breathing primacy hypothesis.
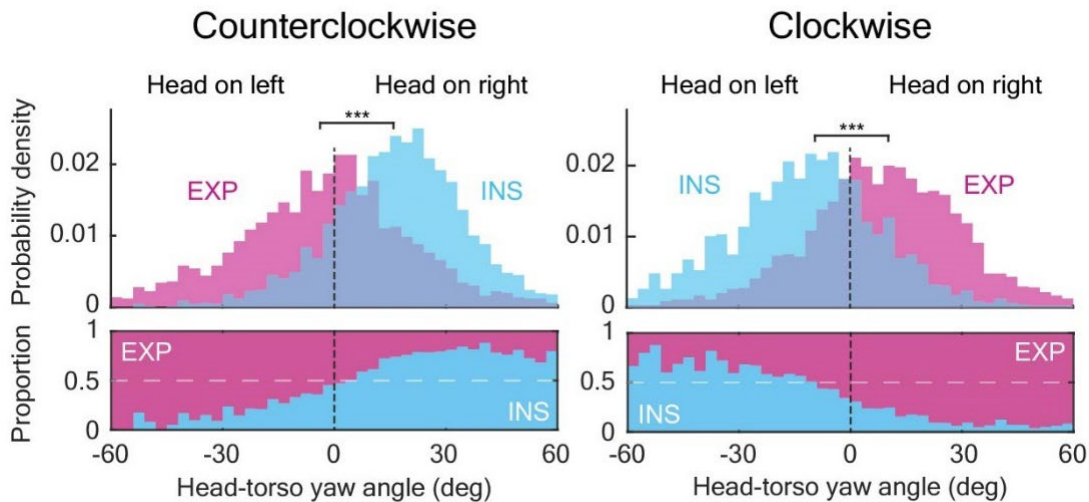
Figure 16: **(Top)** Probability density distributions of head-torso yaw angle of INS and EXP head scans in CCW (left) and CW (right) directions. **(Bottom)** The proportion of INS and EXP head scans as a function of the head-torso yaw angle.
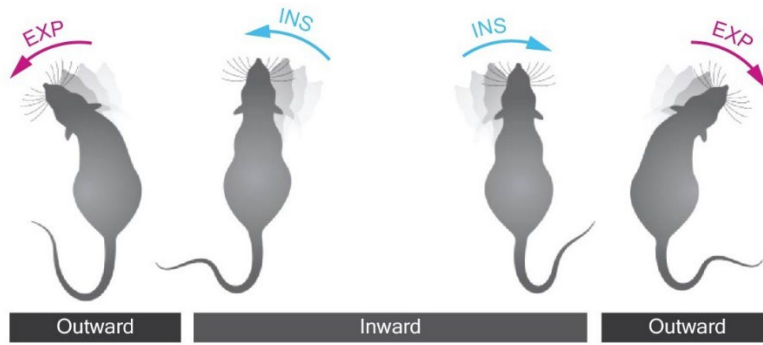
Figure 17: Illustration of the preferred respiratory phases (INS or EXP) of inward and outward head scans.
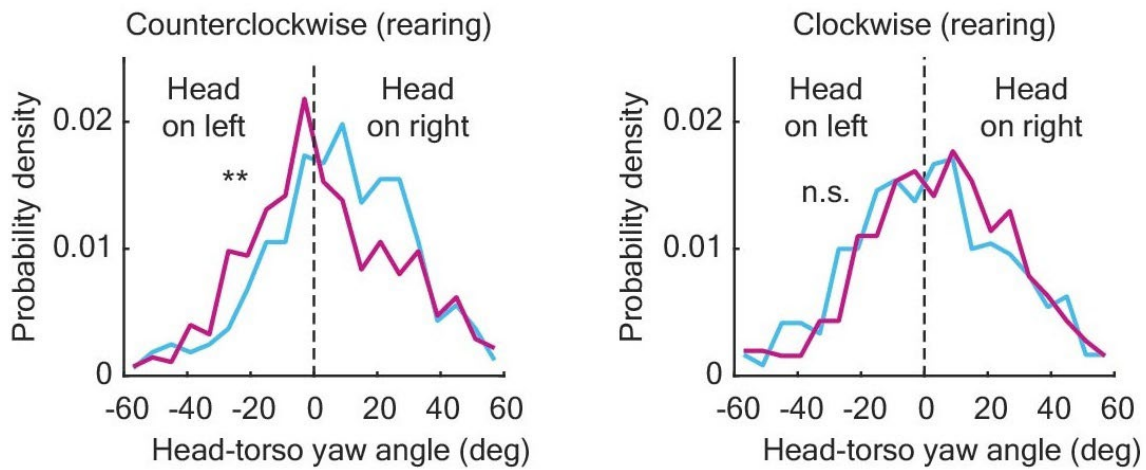
Figure 18: Probability density distributions of head-torso yaw angle of INS and EXP head scanning in CCW (left) and CW (right) directions during rearing. Data pooled from 17 animals.

3.4 Allocentric heading control

In this section, we discuss the control of heading in the allocentric coordinates, i.e., in the arena's coordinates. Foraging is a process where the animal needs to increase the encounter rate with the food source (Viswanathan et al., 2011). The pattern of its heading control in the allocentric coordinates might reflect the animal's navigational strategy to search for food pellets whose location is unknown. If the animal doesn't change its heading, the trajectory will be a straight line,

and the animal will frequently miss the food pellet that is just a little deviated from its current path. On the other hand, if the animal takes turns too frequently, it will waste much of its efforts revisiting the same locations that contain no food source. To delineate the dynamics of the allocentric heading control, we plot the absolute value of the turning angle of the head at varying lengths of the temporal step size (Figure 19A, n = 33). The mean of the heading difference is 6.7° at the sniffing (or head scanning) timescale (0.1 seconds) and 13.9° at the basal breathing (or orientation) timescale (0.25 seconds).

To further study the dynamics of allocentric heading at different timescales, we can take the turning angle as a diffusion process and plot the mean squared turning angles at different lengths of the temporal step size in a log-log scale plot (Figure 19B, n = 33). The Hurst exponent (H), defined as the half of the slope on the log-log plot, characterizes the diffusion process of the turning angle during foraging (Viswanathan et al., 2011). The diffusion is ballistic when H = 1 and Brownian when H = 0.5. From our foraging data (Figure 19B), we see that the Hurst exponent varies at different timescales. The diffusional property of the allocentric heading is close to ballistic at sniffing timescales and becomes more diffusive at longer timescales. This is a characteristic feature of a correlated random walk, where the animal holds a "directional memory" that dissipates at timescales longer than the correlation time (Viswanathan et al., 2005; Viswanathan et al., 2011).

We follow the framework developed by Viswanathan et al. (Viswanathan et al., 2005; Viswanathan et al., 2011) and assume that the rat's locations at two subsequent time steps (size of the time step is denoted by t_0) are $\mathbf{r}_i$ and $\mathbf{r}_{i+1}$, with a turning angle of θ. The two-point correlation function of a single time step is:

$$C(1) = \frac{<\mathbf{r}_i \cdot \mathbf{r}_{i+1}>}{<r_i \, r_{i+1}>} = \frac{<r_i \, r_{i+1} \cos\theta>}{<r_i \, r_{i+1}>}$$

Under the assumption that the step size of the locomotion and the turning angle of the head are sampled from mutually independent and identically distributions, the correlation function can be written as (Viswanathan et al., 2005; Viswanathan et al., 2011):

$$C(1) = <cos\theta>$$

Because of the Markovian property, the correlation function over multiple time steps (t = Nt_0) is (Viswanathan et al., 2005; Viswanathan et al., 2011):

$$C(N) = C(1)^{\frac{t}{t_0}} = e^{\frac{t}{t_0}ln<cos\theta>} \equiv e^{-\frac{t}{\tau}}$$

The correlation time (τ) can be viewed as the lifetime of the correlation of the turning angles (Viswanathan et al., 2005; Viswanathan et al., 2011). We estimate it from our data by plotting the mean (across all trials and animals) of the cosine of the turning angle, as a function of varying temporal time steps. Figure 19C shows the results from 33 rats. The correlation is close to 1.0 at small timescales, meaning that the rat tends to remain and correlate the heading to its current heading (directional memory). The correlation drops below 0.9 at the step size of 1.5 seconds. Therefore, the correlation time (τ) of the turning angle (i.e., the lifetime that the directional memory lasts) is:

$$\tau = -\frac{t_0}{\ln <cos\theta>} = -\frac{1.5}{\ln(0.9)} \sim 14.2\ seconds$$
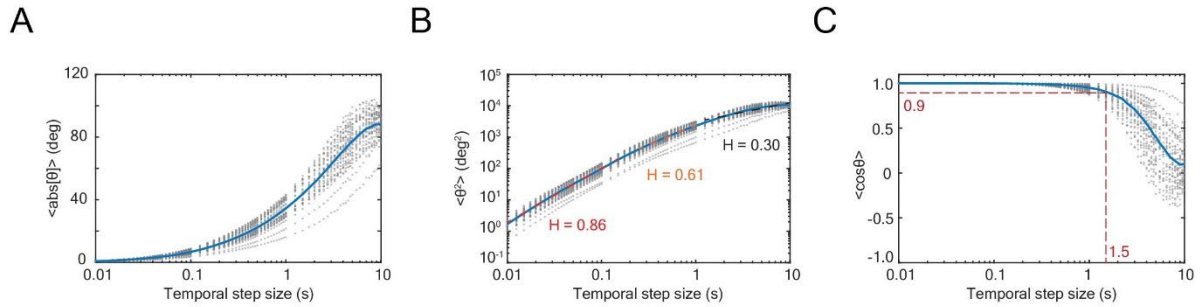
Figure 19: **(A)** Mean absolute turning angle at different unit step sizes **(B)** Mean squared turning angle at different unit step sizes. The Hurst exponents are fitted at the sniffing (0.01-0.15 s, red), basal breathing (0.25-1.0 s, orange), and macroscopic (1.25-10 s, black) timescales. **(C)** Mean cosine of turning angle at different unit step sizes. Data pooled from 33 animals.

Acknowledgements

Chapter 4. Neck muscle recruitment and modeling

In the previous chapter, we delineate the bimodal coordination of the horizontal head movement with breathing, i.e., inspiratory inward head scanning and expiratory outward head scanning. However, the signals from the head and torso sensors only give us the resultant movement from the net torque exerted by all neck muscles. It's still unknown whether the commands of the two respiratory modes (inspiratory and expiratory) descend to the same neck muscle or different muscles. To better understand the control of the head movement at the level of neural circuitry, it's crucial to delineate the pattern of the final motor outputs from the neck musculature. In this chapter, we delineate the recruitment of the neck muscles during the foraging and rearing states. At the end of this chapter, we discuss some computational models that provide insights into understanding the connections and functionality of the brainstem circuitry that patterns the head movement.

4.1 Electromyogram recordings in neck muscles

The posture and movement of the head in the three-dimensional space involve at least 14 pairs of neck muscles (Bekele, 1983). In this work, we report the electromyogram (EMG) recordings from five selected muscles (Figure 20) due to the feasibility of surgical procedures and the well-studied understanding of the locations of motoneuron pools and compositional types of their muscle fibers (Brichta et al., 1987; Callister et al., 1987). We record EMGs from three ventrolateral neck muscles: sternomastoid (SM), cleidomastoid (CM), and clavotrapezius (CT), as well as two dorsal neck muscles: splenius (SP) and biventer cervicis (BC). Figure 21 shows the example data of the EMG signals from the five neck muscles during foraging.

Cross-correlations of the EMG envelopes with the head (or head-torso) movements confirm the roles of all five muscles in the horizontal head control (Figure 22, Figure 23). The coherence analysis of the neck EMG envelopes with the head yaw velocity (Figure 24) shows that all the five muscles are phase-locked to heading in the allocentric coordinates. We find muscle SM has the weakest coherence with the horizontal movement of the head (but is still above the 95% confidence interval). The coherence of the neck EMGs with the head-torso yaw velocity shows that four (CM, CT, SP, and BC) of the five muscles are coherent with the egocentric horizontal head movement (Figure 24).
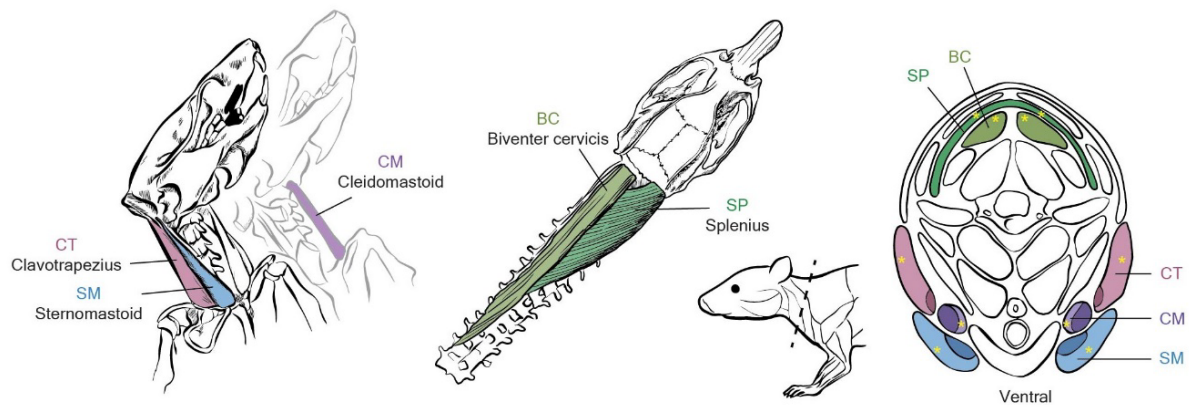
Figure 20: **(Left)** Illustration of ventral neck muscles sternomastoid (SM), cleidomastoid (CM) and clavotrapezius (CT). **(Middle)** Illustration of dorsal neck muscles splenius (SP) and biventer cervicis (BC). **(Right)** Coronal section showing the relative locations of the muscles. Figures adapted from Brichta et al., 1987 and Callister et al., 1987. Yellow asterisks indicate the approximate locations where the electromyogram (EMG) is recorded.
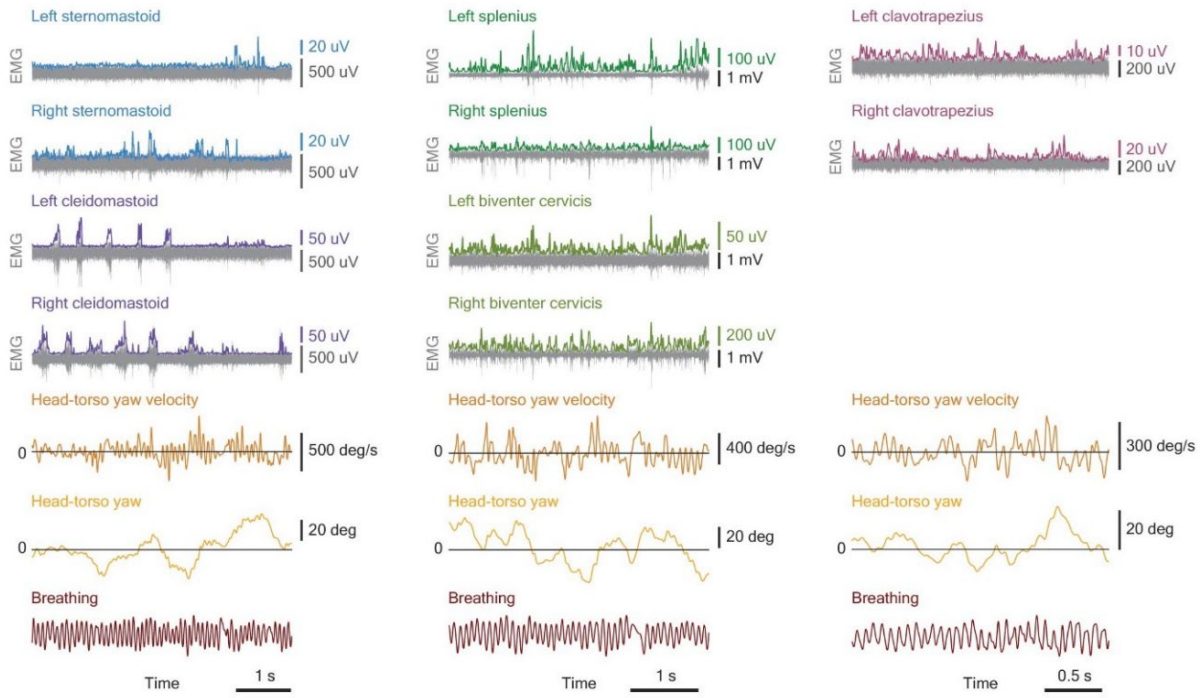
Figure 21: Example data of neck EMG signals along with head movements and breathing. Each column corresponds to an animal.
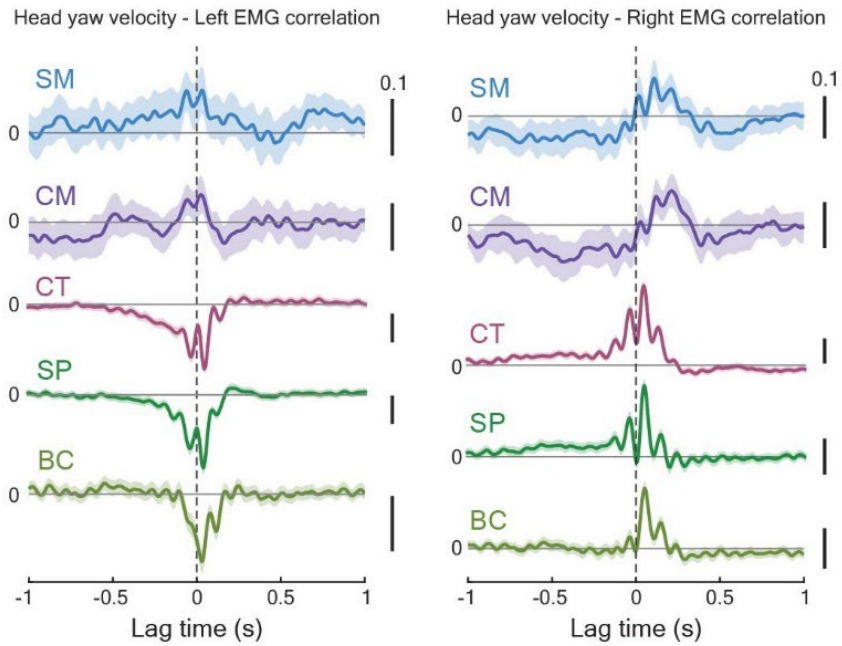
Figure 22: Correlation of head yaw velocity with EMG peaks in the left and right sides of neck muscles. Standard errors are shown. Correlation averaged from windows of size 4 seconds (SM/CM: 34 windows from one animal, CT: 152 windows from one animal, SP/BC: 144 windows from one animal).
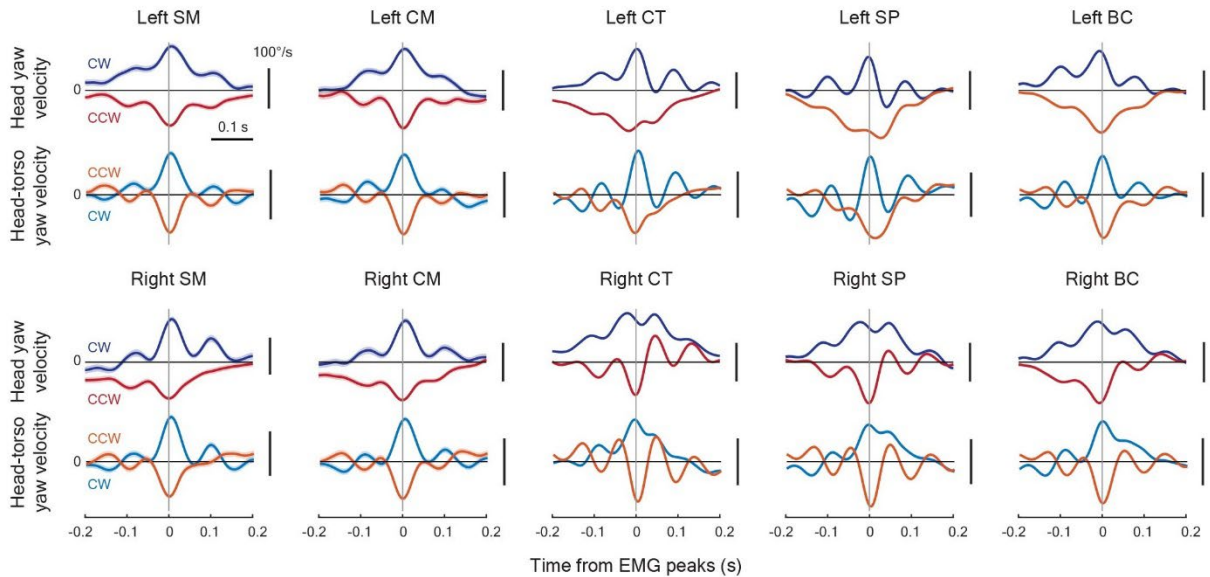
Figure 23: Correlation of head (and head-torso) yaw velocity with neck EMG peaks.
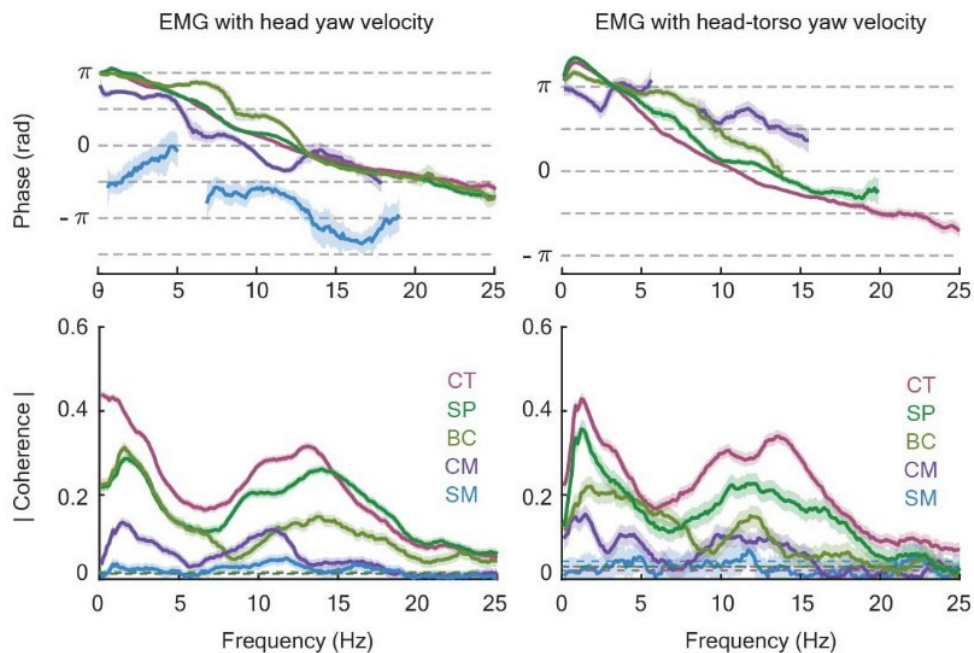
Figure 24: **(Left)** Coherence of neck EMG envelopes with head yaw velocity. Data pooled from SM: 7, CM: 8, CT: 11, SP: 10, BC: 7 animals. **(Right)** Coherence of neck EMG envelopes with head-torso yaw velocity. Data pooled from SM: 2, CM: 3, CT: 4, SP: 3, BC: 3 animals.

The activities of all five neck muscles are correlated with breathing during foraging and rearing (Figure 25, Figure 26). We find that (1) the five neck muscles can be categorized into two subgroups that are correlated with sniffing at distinct phases and (2) the preferred respiratory phase of each subgroup shifts as the animal switches between the foraging and rearing states. The first subgroup consists of muscles SM and CM, which are recruited at the expiratory phase of sniffing during foraging and at the inspiratory phase during rearing. The other subgroup consists of muscles CT, SP, and BC, which are recruited at the inspiratory phase of sniffing during foraging and at the expiratory phase during rearing (Figure 25, Figure 26). The coherence analysis confirms that the neck EMG envelopes are phase-locked to sniffing during both foraging and rearing (Figure 27).

The phase-locking is accompanied by (1) a change in the entrainment frequency that is consistent with the frequency shift in sniffing between the two states (Figure 9) and (2) a shift of

~π radians relative to the sniffing rhythm (except for muscle CT whose phase shift is ~π/2 radians) between the two states (Figure 27).
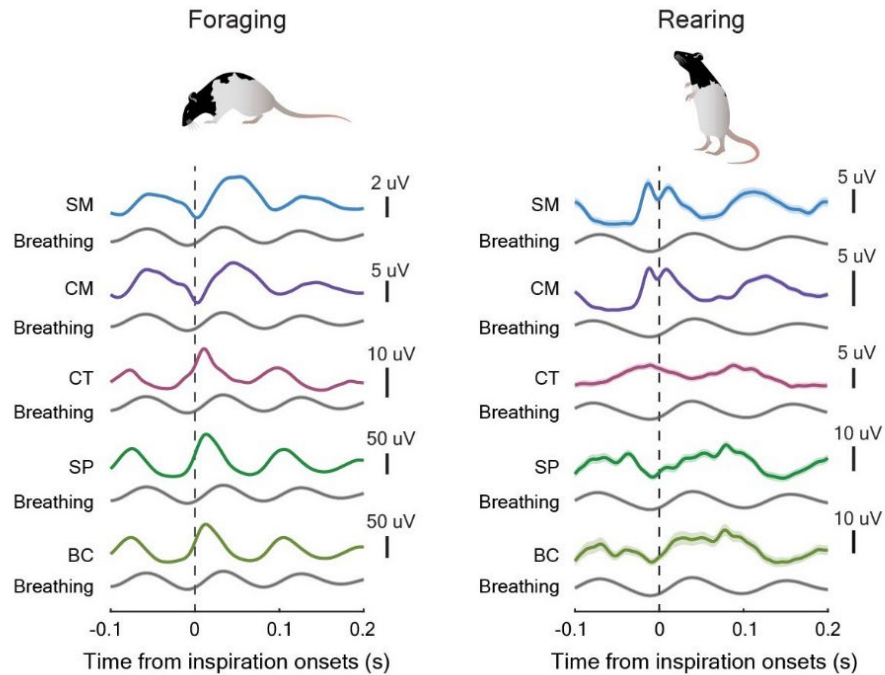
Figure 25: Cross-correlation of neck EMG envelopes with the inspiration onsets in the foraging (left) and rearing (right) states. The standard errors are shown. Data from individual animals. Number of inspiration onsets (foraging/rearing): SM (10,932/990), CM (7,513/2,645), CT: (7,486/1,658), SP: (13,686/1,572), and BC: (14,805/473).
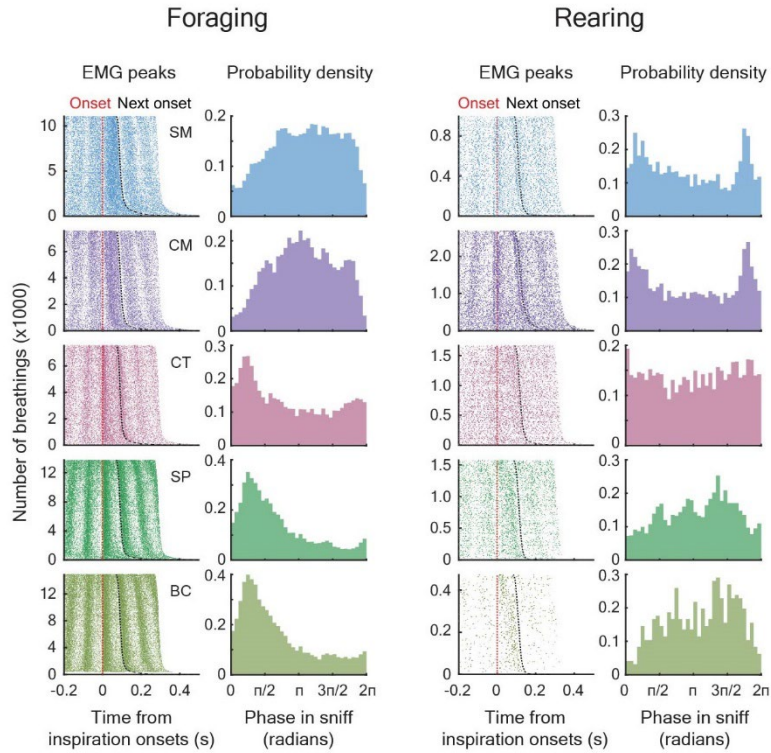
Figure 26: Raster plots of the neck EMG peaks with respect to the inspiration onsets and the probability density distributions of the phases in the sniffing cycle in the foraging (left) and rearing (right) states. Data from individual animals.
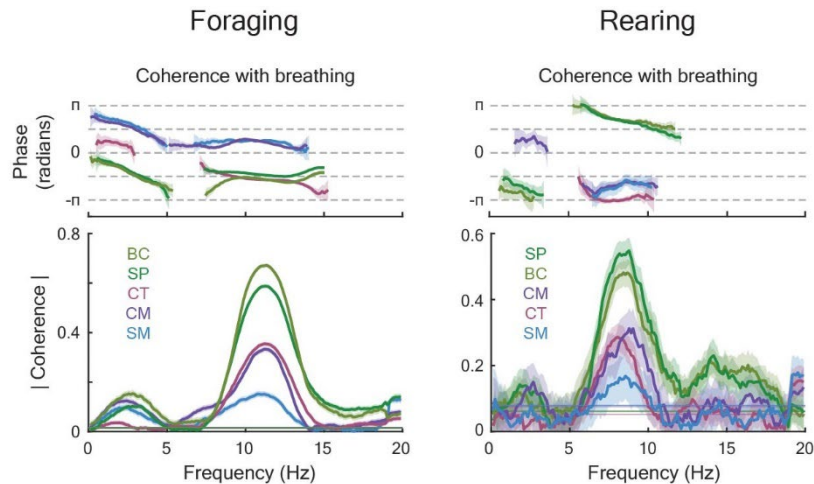
Figure 27: Coherence of the neck EMG envelopes with breathing in the foraging (left) and rearing (right) states. Coherence averaged from segments of size 4 seconds, with half-bandwidth of 1 Hz and 7 tapers. Data pooled from SM: 7, CM: 8, CT: 11, SP: 10, and BC: 7 animals. Number of segments (foraging/rearing): SM (1,803/67), CM (2,039/74), CT (3,013/158), SP (2,557/110), BC (1,435, 115).

4.2 Head scanning and orientation by neck muscles

Combined with the results in Chapter 3.3, we can illustrate the synergistic motor control of head scanning as the rat forages in Figure 28. After the inspiration onset, muscles CT, BC, and SP are recruited during inhalation. In the meantime, the scanning is more likely to be inward. After maximal inhalation, the sniff cycle enters expiration, where muscles SM and CM are recruited to drive the head during exhaling. In the meantime, the scanning is more likely to be outward. With the completion of the sniff cycle, the rat completes a round of head scanning of its peri-personal space (Figure 28).
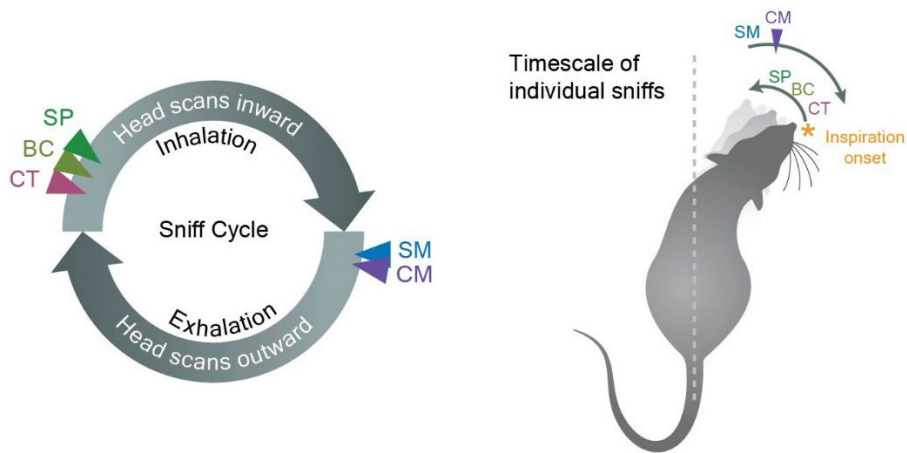
Figure 28: Depiction of head scanning with sequential activation of the neck muscles.

We identify an additional role of the muscle cleidomastoid (CM) by plotting the cross-correlation between the left and right muscles (Figure 29). In addition to the correlation at the time delay of zero (bilateral co-activation), CM also shows a peak at around $\pm$ 0.25 seconds, the timescale of head orientation (Figure 8). Therefore, CM is also responsible for the control of head orientation. At the timescale of multiple sniffing, unilateral CM is continuously activated to drive

the head to the ipsilateral side. In the meantime, the EMG envelope consists of multiple peaks individually synchronizing with each sniffing cycle (Figure 30). This can be observed from the example data shown in Figure 21. All the other four neck muscles (SM, CT, SP, and BC) exhibit bilateral co-activation (Figure 29). The net torque from all neck muscles on both sides of the rat determines the resultant direction of the heading.
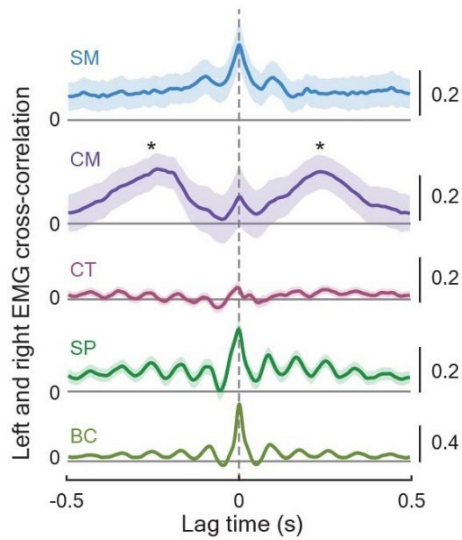
Figure 29: Cross-correlation of the left and right neck muscles. Asterisks mark the activities related to head orientation in cleidomastoid (CM).
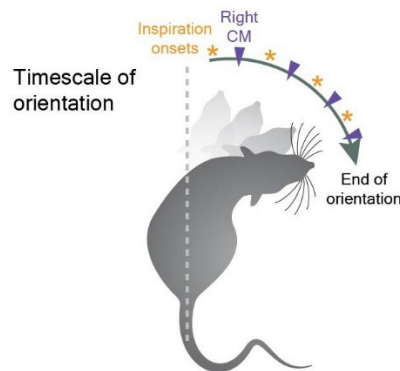
Figure 30: Illustration of head orientation with ipsilateral cleidomastoid (CM) activation.

4.3 Model of weakly coupled oscillators: reciprocal coupling

We now turn to our experimental observation that in the neck muscles (SM, CM, SP, and BC), there is a phase (with respect to breathing) shift of ~π radians as the rat switches between the foraging and rearing states (Figure 27). The phase difference between the neck activities and breathing depends on the behavioral mode and is accompanied by a shift in the sniffing frequency (Figure 9). The phenomenon can be explained by a computational model with two weakly coupled phase oscillators with a propagation time delay (Kuramoto, 1984; Kopell and Ermentrout, 1986; Kopell, 1988; Schuster and Wagner, 1989; Ermentrout and Kleinfeld, 2001; Figure 31).
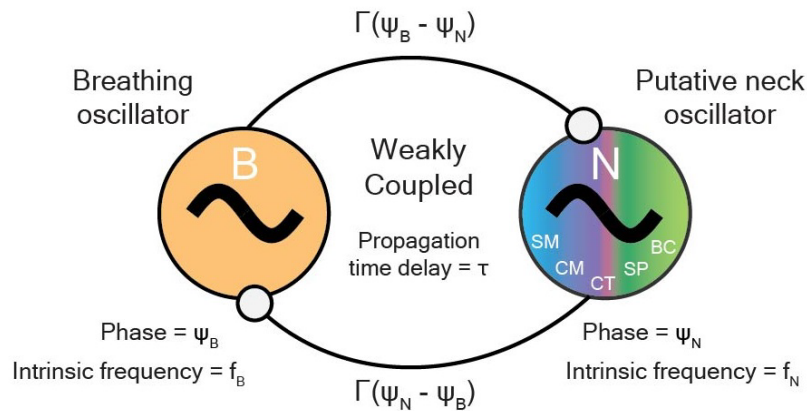
Figure 31: Weakly coupled oscillators with reciprocal connections.

The model of weakly coupled oscillators has been applied to study the traveling waves in lamprey's spinal cord, Mollusk's olfactory lobe, and the cortex activity in cats (Cohen et al., 1982; Kuramoto, 1984; Kopell and Ermentrout, 1986; Delaney et al., 1994; Roelfsema et al., 1997; Ermentrout and Kleinfeld, 2001). In the model, two oscillators are coupled reciprocally by mutual interactions. One is the breathing oscillator, and the other is the putative neck oscillator that patterns the activities of all neck motoneurons. We use a single variable, the phase (Ψ_B and Ψ_N),

to represent the set of the oscillator's state variables (e.g., the membrane potential and the gating variables of the ion channels) on its limit cycle. Each oscillator has its intrinsic frequency (denoted by f_B and f_N in Hz or by ω_B and ω_N in radian/s), which is the rate of the oscillation if there's no external perturbation. The coupling between the two oscillators is weak, meaning that the interaction is only big enough to affect each other's phase and timing on its limit cycle but is not strong enough to change the shape of the limit cycle (Kuramoto, 1984; Kopell and Ermentrout, 1986; Kopell, 1988; Ermentrout and Kleinfeld, 2001).

We follow the framework and derivation by Schuster and Wagner (Schuster and Wagner, 1989) by assuming that the interaction is symmetric and takes a form that depends on the phase difference between the two oscillators:

$$\Gamma(\Psi_B - \Psi_N) = \Gamma_0 \sin(\Psi_B - \Psi_N)$$

$$\Gamma(\Psi_N - \Psi_B) = \Gamma_0 \sin(\Psi_N - \Psi_B)$$

With this form of reciprocal interaction and a propagational time delay τ, we can write down the following equations that govern the phases of the two oscillators (Schuster and Wagner, 1989):

$$\frac{d}{dt}\Psi_N(t) = \omega_N + \Gamma_0 \sin[\Psi_B(t-\tau) - \Psi_N(t)] \quad (1)$$

$$\frac{d}{dt}\Psi_B(t) = \omega_B + \Gamma_0 \sin[\Psi_N(t-\tau) - \Psi_B(t)] \quad (2)$$

In Eq (1) and Eq (2), ω_N and ω_B are the intrinsic angular frequencies (in radian/s) of the two oscillators. They are given by:

$$\omega_N = 2\pi f_N$$

$$\omega_B = 2\pi f_B$$

When the two oscillators are phase-locked, we have:

$$\frac{d}{dt}\Psi_N(t) = \frac{d}{dt}\Psi_B(t)$$

We use Ω to denote the angular frequency at which the two oscillators are entrained. This is the frequency that we can measure by experiments. We use α to denote the constant phase difference of the neck oscillator relative to the breathing oscillator ($\alpha \equiv \Psi_N - \Psi_B$) when they are phase locked. A positive α means the neck oscillator lags the breathing oscillator and vice versa. With these notations, we can write (Schuster and Wagner, 1989):

$$\Psi_N(t) = \Omega t + \frac{\alpha}{2} \quad (3)$$

$$\Psi_B(t) = \Omega t - \frac{\alpha}{2} \quad (4)$$

Substituting Eq. (3) and Eq. (4) into Eq. (1) and Eq. (2), we have:

$$\Omega = \omega_N - \Gamma_0 \sin(\Omega\tau + \alpha) \quad (5)$$

$$\Omega = \omega_B - \Gamma_0 \sin(\Omega\tau - \alpha) \quad (6)$$

Solving equations (5) and (6) arithmetically for Ω and α, we can obtain the following expression for Ω (formatted as in Schuster and Wagner, 1989):

$$f(\Omega) \equiv \frac{\omega_N + \omega_B}{2} - \Omega - \Gamma_0 \tan(\Omega\tau) \sqrt{\cos^2(\Omega\tau) - \frac{(\omega_N - \omega_B)^2}{4\Gamma_0^2}} = 0 \quad (7)$$

The solution of Ω can be found numerically by finding the intersection(s) of $f(\Omega)$ in Eq. (7) with the x-axis. Once we obtain Ω, we can solve for the phase difference α based on the sign of $\cos(\Omega\tau)$ (Schuster and Wagner, 1989):

If $\cos(\Omega\tau) > 0$,

$$\alpha = \sin^{-1}(\frac{\omega_N - \omega_B}{2\Gamma_0 \cos(\Omega\tau)})$$

Otherwise,

$$\alpha = \pi - \sin^{-1}\left(\frac{\omega_N - \omega_B}{2\Gamma_0 \cos(\Omega\tau)}\right)$$

From our experiments, we observe $\Omega \sim 22\pi$ radian/s (11 Hz) when the rat is foraging and $\Omega \sim 16\pi$ radian/s (8 Hz) when the rat is rearing. We note that for the phase difference between the two oscillators to shift, we need to have the signs of $\cos(\Omega\tau)$ be opposite between the two states, i.e.,

$$16\pi\ \tau < \frac{(2n-1)\pi}{2} < 22\pi\ \tau, \ \ n = 1, 2, 3, \dots$$

When n = 1 or 2, we can obtain the propagation time delays that are less than 100 msec (τ is in [22.73, 31.25] msec for n = 1 and in [68.18, 93.75] msec for n = 2). We don't consider propagation time delays that are longer than 100 milliseconds.

We further assume that the intrinsic frequency of the neck oscillator is 19π radian/s (9.5 Hz). We restrict the coupling strength (Γ_0) in the range of [1, 10] (in Hz) and solve for ω_B and Γ_0 with varying propagation time delays (τ) such that the two oscillators can be phase locked at 8 Hz and 11 Hz. We find that when the time delay is in the range of [22.73, 31.25] msec, we can only generate a phase shift ranging approximately from 0.02π ($\tau = 25.1$ msec) to 0.44π ($\tau = 30.4$ msec). These values are not close to our experimental data, where we observe the phase shift to be about π radians.

When the time delay is in the range of [68.18, 93.75] msec, we can generate a phase shift ranging from 0.29π ($\tau = 88$ msec) to 0.82π ($\tau = 79.9$ msec). We show the solution with $\tau = 79.9$ msec in Figure 32, where we plot $f(\Omega)$ (see Eq. (7)) for the foraging and rearing states. The two curves intersect with the x-axis at 11 Hz (foraging) and 8 Hz (rearing) respectively. When the intrinsic frequency of breathing is 20.6π radian/s (10.3 Hz) with the coupling strength $\Gamma_0 = 3.38\pi$ radian/s (1.69 Hz), the two oscillators are phase-locked at 11 Hz with a phase difference of -0.107π

(two oscillators are almost in phase). When the intrinsic frequency of breathing shifts to 18π radian/s (9 Hz) with the coupling strength $\Gamma_0 = 3.34\pi$ radian/s (1.67 Hz), the two oscillators are phase-locked at 8 Hz with a phase difference of -0.922π (two oscillators are almost in anti-phase). The net phase shift between the two states is approximately 0.815π radians (Figure 32, bottom panel). This phase shift is close to what we observe experimentally.
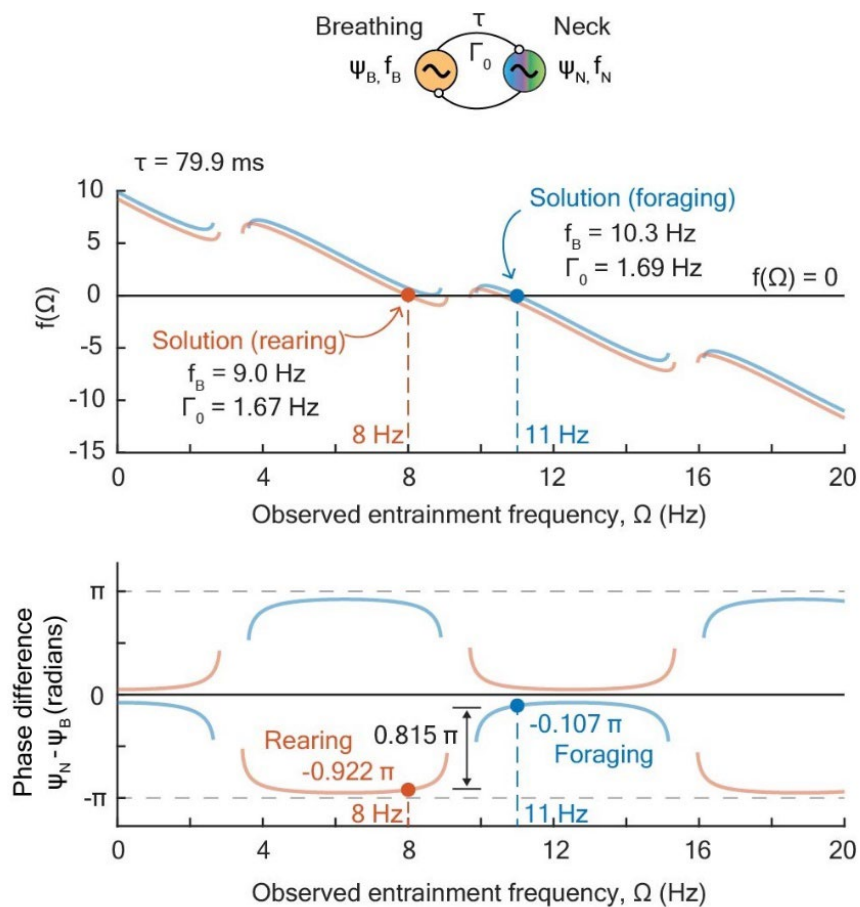
Figure 32: A solution to the reciprocal coupling model for head movement. **(Top)** The function $f(\Omega)$ (Eq. 7) in the foraging (blue) and rearing (red) states. Their intersections with the x-axis are the frequencies at which the two oscillators are locked. **(Bottom)** The phase difference of the neck oscillator from the breathing oscillator.

45

We can infer the stability of the solutions by the linear stability analysis (Schuster and Wagner, 1989). We add small perturbations to the equilibrium solutions:

$$\Psi_N(t) = \Psi_N^{Eq}(t) + \xi_N(t) \quad (8)$$

$$\Psi_B(t) = \Psi_B^{Eq}(t) + \xi_B(t) \quad (9)$$

The perturbations ξ_N and ξ_B take the forms:

$$\xi_N(t) \propto e^{\lambda t}$$

$$\xi_B(t) \propto e^{\lambda t}$$

The assumption on the form of the perturbations indicates two properties. First, with the propagation time delay we have:

$$\xi_N(t - \tau) = e^{-\lambda \tau} \xi_N$$

$$\xi_B(t - \tau) = e^{-\lambda \tau} \xi_B$$

Second, by taking the time derivatives,

$$\frac{d}{dt} \begin{bmatrix} \xi_N(t) \\ \xi_B(t) \end{bmatrix} = \lambda \begin{bmatrix} \xi_N(t) \\ \xi_B(t) \end{bmatrix}$$

By substituting Eq. (8) and Eq. (9) into Eq. (1) and Eq. (2), we obtain:

$$\frac{d}{dt} \Psi_N^{Eq}(t) + \frac{d}{dt} \xi_N(t) = \omega_N + \Gamma_0 \sin\left[\Psi_B^{Eq}(t - \tau) + \xi_B(t - \tau) - \Psi_N^{Eq}(t) - \xi_N(t)\right]$$

$$= \omega_N + \Gamma_0 \sin\left[\Psi_B^{Eq}(t - \tau) - \Psi_N^{Eq}(t) + e^{-\lambda \tau} \xi_B(t) - \xi_N(t)\right]$$

$$\frac{d}{dt} \Psi_B^{Eq}(t) + \frac{d}{dt} \xi_B(t) = \omega_B + \Gamma_0 \sin\left[\Psi_N^{Eq}(t - \tau) + \xi_N(t - \tau) - \Psi_B^{Eq}(t) - \xi_B(t)\right]$$

$$= \omega_B + \Gamma_0 \sin\left[\Psi_N^{Eq}(t - \tau) - \Psi_B^{Eq}(t) + e^{-\lambda \tau} \xi_N(t) - \xi_B(t)\right]$$

By assuming that the perturbation terms are small, we expand the last term in both equations and obtain:

$$\frac{d}{dt} \Psi_N^{Eq}(t) + \frac{d}{dt} \xi_N(t) = \omega_N + \Gamma_0 \sin\left[\Psi_B^{Eq}(t - \tau) - \Psi_N^{Eq}(t)\right] + \Gamma_0 \cos\left[\Psi_B^{Eq}(t - \tau) - \Psi_N^{Eq}(t)\right]\left[e^{-\lambda \tau} \xi_B(t) - \xi_N(t)\right]$$

$$\frac{d}{dt} \Psi_B^{Eq}(t) + \frac{d}{dt} \xi_B(t) = \omega_B + \Gamma_0 \sin\left[\Psi_N^{Eq}(t - \tau) - \Psi_B^{Eq}(t)\right] + \Gamma_0 \cos\left[\Psi_N^{Eq}(t - \tau) - \Psi_B^{Eq}(t)\right]\left[e^{-\lambda \tau} \xi_N(t) - \xi_B(t)\right]$$

The equilibrium solutions satisfy Eq. (1) and Eq. (2):

$$\frac{d}{dt}\Psi_N^{Eq}(t) = \omega_N + \Gamma_0 \sin\left[\Psi_B^{Eq}(t-\tau) - \Psi_N^{Eq}(t)\right]$$

$$\frac{d}{dt}\Psi_B^{Eq}(t) = \omega_B + \Gamma_0 \sin\left[\Psi_N^{Eq}(t-\tau) - \Psi_B^{Eq}(t)\right]$$

We therefore have:

$$\frac{d}{dt}\xi_N(t) = \Gamma_0 \cos\left[\Psi_B^{Eq}(t-\tau) - \Psi_N^{Eq}(t)\right]\left[e^{-\lambda\tau}\xi_B(t) - \xi_N(t)\right]$$

$$\frac{d}{dt}\xi_B(t) = \Gamma_0 \cos\left[\Psi_N^{Eq}(t-\tau) - \Psi_B^{Eq}(t)\right]\left[e^{-\lambda\tau}\xi_N(t) - \xi_B(t)\right]$$

With Eq. (3) and Eq. (4), we obtain:

$$\frac{d}{dt}\xi_N(t) = \Gamma_0\cos(\Omega\tau + \alpha)\left[-\xi_N(t) + e^{-\lambda\tau}\xi_B(t)\right]$$

$$\frac{d}{dt}\xi_B(t) = \Gamma_0\cos(\Omega\tau - \alpha)\left[e^{-\lambda\tau}\xi_N(t) - \xi_B(t)\right]$$

We can rewrite it as:

$$\frac{d}{dt}\begin{bmatrix}\xi_N(t)\\\xi_B(t)\end{bmatrix} = \begin{bmatrix}-\Gamma_0\cos(\Omega\tau + \alpha) & \Gamma_0 e^{-\lambda\tau}\cos(\Omega\tau + \alpha)\\\Gamma_0 e^{-\lambda\tau}\cos(\Omega\tau - \alpha) & -\Gamma_0\cos(\Omega\tau - \alpha)\end{bmatrix}\begin{bmatrix}\xi_N(t)\\\xi_B(t)\end{bmatrix} \equiv M\begin{bmatrix}\xi_N(t)\\\xi_B(t)\end{bmatrix}$$

The stability of the above differential equations can be inferred by solving the eigenvalues

of the matrix M (Schuster and Wagner, 1989):

$$det\begin{bmatrix}-\Gamma_0\cos(\Omega\tau + \alpha) - \lambda & \Gamma_0 e^{-\lambda\tau}\cos(\Omega\tau + \alpha)\\\Gamma_0 e^{-\lambda\tau}\cos(\Omega\tau - \alpha) & -\Gamma_0\cos(\Omega\tau - \alpha) - \lambda\end{bmatrix} = 0$$

Solutions with negative λ are stable. Solutions of the foraging and rearing states in Figure

32 are found to be unstable. It motivated us to consider the next model (Chapter 4.4).

4.4 Model of weakly coupled oscillators: unidirectional coupling

The previous reciprocal model relies on the assumption that the two oscillators are coupled reciprocally. Although our data show the existence of respiratory drives in the neck muscle activities (Figure 27), it is still unknown whether there is a projection from the neck oscillator to the breathing center. Here we discuss a simpler model with only a unidirectional coupling (Kleinfeld and Mehta, 2006) with a propagation time delay from the breathing oscillator to the neck oscillator but not vice versa (Figure 33).
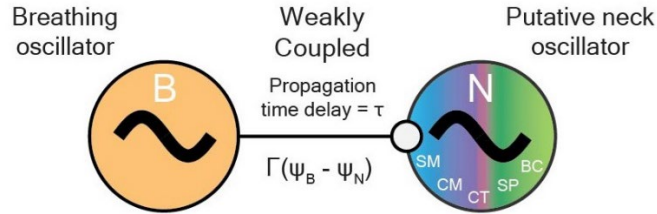
Figure 33: Weakly coupled oscillators with the unidirectional connection.

In the unidirectional model, we can write down the equations of the phases of the two oscillators as follows:

$$\frac{d}{dt}\Psi_N(t) = \omega_N + \Gamma_0 \sin[\Psi_B(t - \tau) - \Psi_N(t)] \quad (10)$$

$$\frac{d}{dt}\Psi_B(t) = \omega_B \quad (11)$$

When the two oscillators are locked, we have:

$$\frac{d}{dt}\Psi_N(t) = \frac{d}{dt}\Psi_B(t) = \omega_B$$

The above equation indicates that the breathing oscillator drives the neck oscillator at the intrinsic breathing frequency ω_B. Again, by assuming that the phases of the two oscillators take the forms of equations (3) and (4), we can solve equations (10) and (11) and obtain:

$$\alpha = \sin^{-1}(\frac{\omega_N - \omega_B}{\Gamma_0}) - \omega_B \tau \quad (12)$$

The solution for phase-locking exists if:

$$\left| \frac{\omega_N - \omega_B}{\Gamma_0} \right| \leq 1 \quad (13)$$

In addition to Eq. (13), we require that the phase difference shifts by π radians between the foraging and rearing states. The unidirectional model gives us a wide range of feasible solutions for the time delay with varying coupling strengths Γ_0 (Figure 34). The minimal coupling strength is $\Gamma_0 = 3.02\pi$ radian/s (1.51 Hz), with a time delay of 12.2 msec. As the coupling strength increases, the time delay and the system stability (see the next paragraph) also increase. The solution Eq. (12) can be interpreted as a straight line on the x-y plane, where the x-axis is the propagation time delay τ, and the y-axis is the phase difference α between the two oscillators. The slope of the line is $-\omega_B$, and the intercept at the y-axis is given by $\sin^{-1}(\frac{\omega_N - \omega_B}{\Gamma_0})$. Figure 34 depicts a solution with the parameters $\omega_N = 19\pi$ radian/s (9.5 Hz), $\Gamma_0 = 3.1\pi$ radian/s (1.55 Hz), and $\tau = 27$ msec, where the two oscillators are phase-locked at 11 Hz during foraging with a phase delay of 0.987π radians (in anti-phase) and are phase-locked at 8 Hz during rearing with a phase difference of -0.013π radians (in phase). This solution yields a total phase shift of π radians between the two behavioral states.
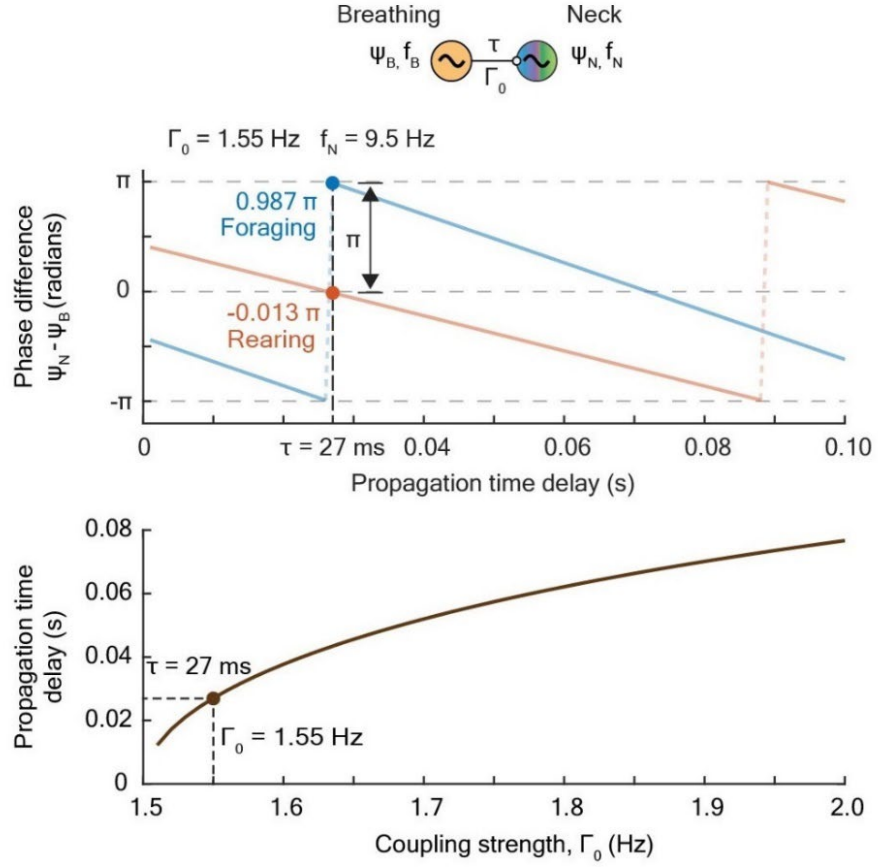
Figure 34: The unidirectional coupling model. **(Top)** The phase difference as a function of the propagation time delay, with the coupling strength = 1.55 Hz, intrinsic neck frequency = 9.5 Hz, and time delay = 27 msec. **(Bottom)** The propagation time delay that yields a phase shift of π radians, as a function of the coupling strength.

The stability of the solutions in the unidirectional model can be inferred by adding a small perturbation to the equilibrium solution of the phase of the neck oscillator.

$$\Psi_N(t) = \Psi_N^{Eq}(t) + \xi_N(t)$$

By substituting into Eq. (10), we have, with Eq. (3) and Eq. (4):

$$\frac{d}{dt}\Psi_N(t) = \frac{d}{dt}\Psi_N^{Eq}(t) + \frac{d}{dt}\xi_N(t) = \omega_N + \Gamma_0 \sin[-\omega_B\tau - \alpha - \xi_n(t)]$$

We can expand the above equation to:

$$\frac{d}{dt}\Psi_N^{Eq}(t) + \frac{d}{dt}\xi_N(t) = \omega_N + \Gamma_0 \sin(-\omega_B\tau - \alpha)\cos(\xi_N(t)) - \Gamma_0\cos(-\omega_B\tau - \alpha)\sin(\xi_N(t))$$

With a small perturbation ($\xi_N(t) \ll 1$):

$$\frac{d}{dt}\Psi_N^{Eq}(t) + \frac{d}{dt}\xi_N(t) = \omega_N - \Gamma_0 \sin(\omega_B\tau + \alpha) - \Gamma_0\cos(\omega_B\tau + \alpha)\xi_N(t)$$

Finally, because the equilibrium solution by its definition satisfies:

$$\frac{d}{dt}\Psi_N^{Eq}(t) = \omega_N - \Gamma_0 \sin(\omega_B\tau + \alpha)$$

We can obtain the following equation for the perturbation:

$$\frac{d}{dt}\xi_N(t) = -\Gamma_0\cos(\omega_B\tau + \alpha)\xi_N(t)$$

We can see that the solution is stable if the term $\cos(\omega_B\tau + \alpha)$ is positive and unstable if $\cos(\omega_B\tau + \alpha)$ is negative. The solutions shown in Figure 34 are stable in both the foraging and rearing states. The stability increases as the coupling strength increases.

4.5 Summary

By directly recording the EMG signals from the neck muscles, we show that the neck muscles are coordinated by multiple phases in the breathing generator during foraging (Figure 25; Figure 26). We show that the phase relationship and frequency of the phase-locking shift between the foraging and rearing states (Figure 27). The observation can be explained by simple computational models of weakly coupled oscillators with reciprocal (Figure 31; Figure 32) or unidirectional (Figure 33; Figure 34) coupling. In both models, the rat can shift the phase of the rhythm of its head movement with respect to breathing by driving its sniffing rhythm at frequencies above or below the intrinsic frequency of the neck oscillator. The observed difference in the sniffing rates during foraging and rearing states might be a means for the rat to switch the phase

relationship of its neck motor outputs to meet any specific behavioral needs or goals with fixed neuronal connections in the brainstem. We will discuss more details and the implications in Chapter 6.

Acknowledgements

Chapter 5. Motor control of vibrissae and nose

We have delineated the bimodal coordination of the heading control with breathing and showed a phase shift that can be explained by simple computation models of weakly coupled oscillators. We now ask whether there are other orofacial motor actions that also show a phase shift with breathing that depends on the behavioral states. In this chapter, we revisit two orofacial motor actions that have been shown to be phase-locked with breathing in past studies – whisking (Moore et al., 2013; Deschênes et al., 2016) and nose twitching (Kurnikova et al., 2017).

5.1 Coordination of vibrissae and nose

To study whisking, we measure the EMG signal from vibrissa intrinsic muscles (VI). VI wraps around the follicle and protracts the vibrissa (Hill et al., 2008; Figure 35). We also record the EMG from the extrinsic muscle nasolabialis (NL), which retracts the vibrissae by pulling back the mystacial pad (Hill et al., 2008; Figure 35). To record the motor action of the nose, we record the EMG from deflector nasi (DN), which is the only muscle that controls the nose movement by drawing it ipsilaterally and upward (Deschênes et al., 2015; Kurnikova et al., 2017; Figure 35).
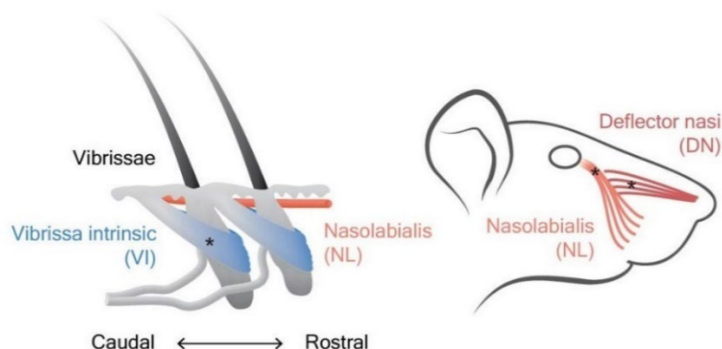
Figure 35: Illustration of the anatomy of vibrissa intrinsic muscles (VI), extrinsic vibrissa retractor nasolabialis (NL), and nose muscle deflector nasi (DN). The anatomical illustration of VI is adapted from Hill et al., 2008.

Figure 36 and Figure 37 show the example EMG data of VI, DN, and NL, along with the head movement and breathing. Their cross-correlation plots with the inspiration onsets are shown in Figure 38 and Figure 39. When the rat is in the rearing state, vibrissae are protracted during inspiration and retracted during expiration, and the nose twitches during expiration. These activation patterns and relative timings are similar to the results in head-fixed rats (Hill et al., 2008; Moore et al., 2013; Kurnikova et al., 2017). Interestingly, as the rat switches to foraging, the activation patterns show differently (Figure 38; Figure 39). VI is still recruited during inspiration but with a wider EMG envelope peak that suggests a prolongation in the activity (n = 3). The activity of NL advances when the rat is in the foraging state (n = 3). The activity in the nose muscle DN becomes inspiratory in the foraging state (n = 7), with two peaks in the EMG envelope during inhaling (Figure 38; Figure 39). Consistent with these findings, the coherence analysis shows that the phase difference of DN relative to breathing shifts approximately by $\pi/2$ radians between the foraging and rearing states, and the phase of NL relative to breathing is advanced by approximately $\pi/4$ radians as the rat switches from rearing to foraging (Figure 40).
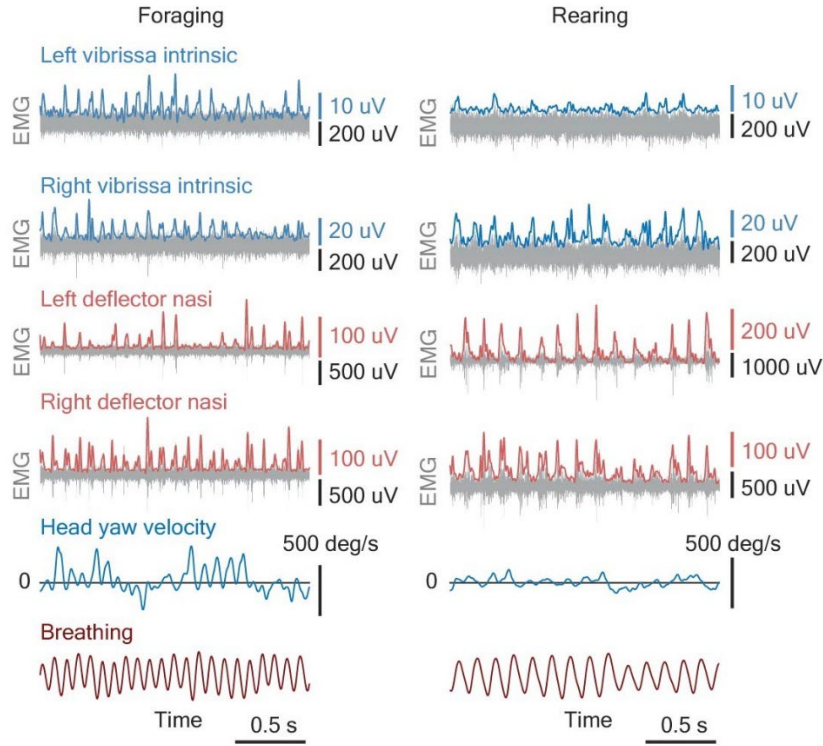
Figure 36: Example data of vibrissa intrinsic (VI) and deflector nasi (DN) EMG recordings.
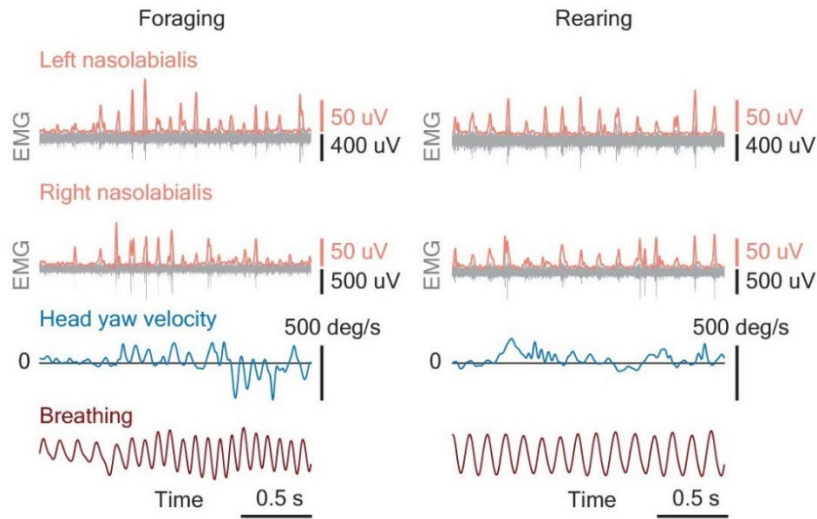
Figure 37: Example data of nasolabialis (NL) EMG recordings.
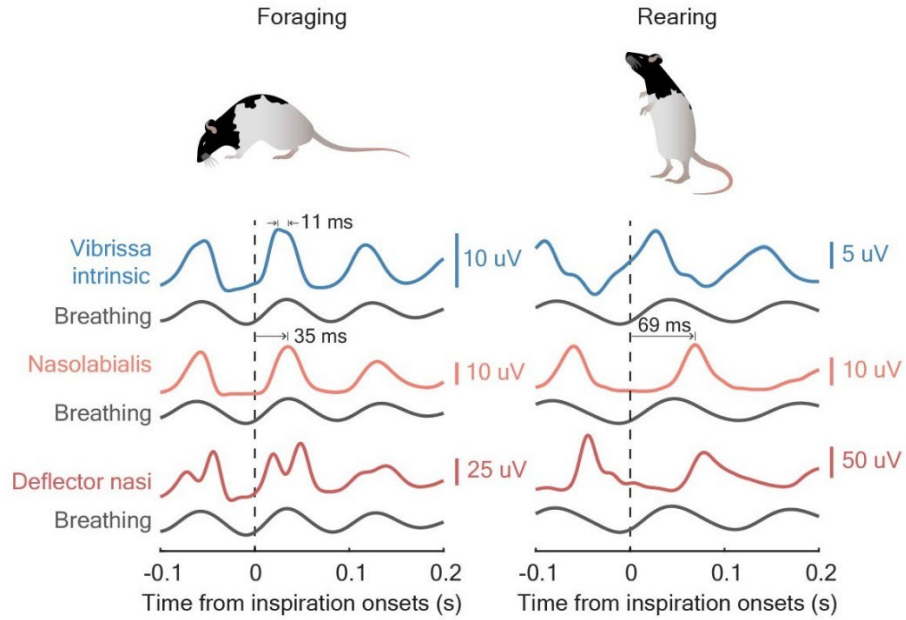
Figure 38: Cross-correlation of vibrissal and nose muscles with inspiration (4 – 14 Hz) onsets. Standard errors are shown. Data from individual animals. Number of inspiration onsets (foraging/rearing): VI (12,852/2,763), NL (11,702/1,133), and DN (10,791/3,450).
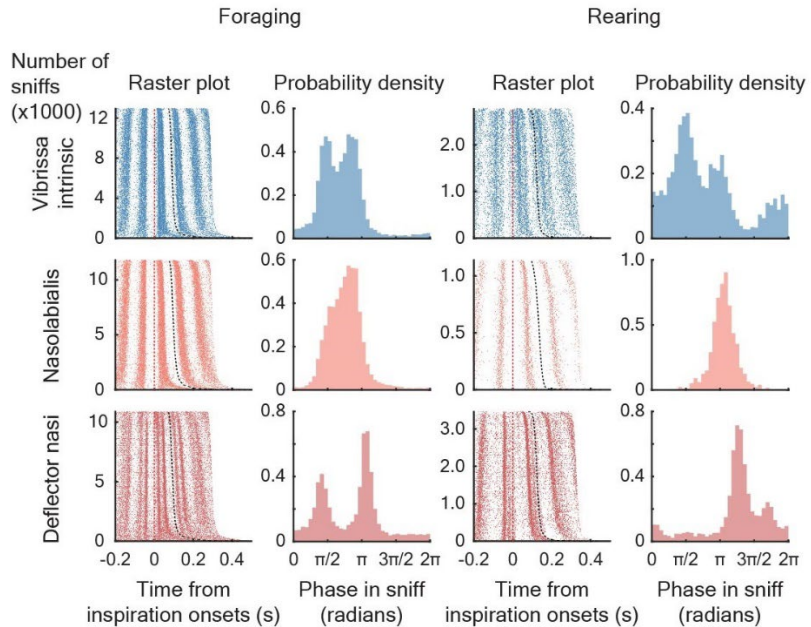
Figure 39: Raster plots of the peaks in vibrissal and nose EMG envelopes with respect to inspiration onsets and the probability density distributions in the sniff (4 – 14 Hz) cycle during the foraging (left two columns) and rearing (right two columns) states.
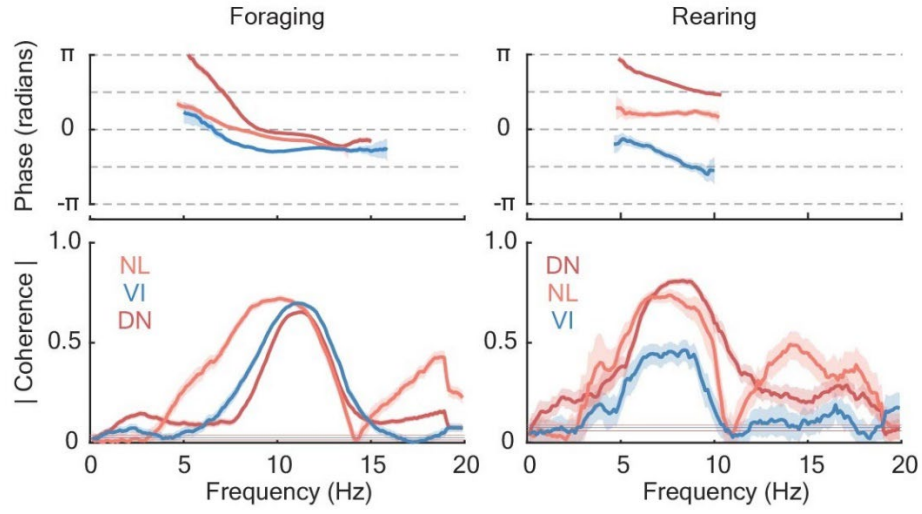
Figure 40: Coherence of VI, NL, and DN EMG envelopes with breathing in the foraging and rearing states (4-second windows, half-bandwidth = 1 Hz, with 7 tapers). Data pooled from VI: 5, NL: 3, DN: 7 animals. Shaded areas indicate the standard errors (Jackknife). The horizontal lines show the 95% confidence levels.

5.2 Computational models for nose-twitching

The phase difference between the EMG of the nose muscle deflector nasi (DN) and breathing is approximate -0.062π radians at 11 Hz during foraging and 0.586π radians at 8 Hz during rearing (n = 7, Figure 40). This gives a total phase shift of 0.648π radians between the two states. With the same framework (Schuster and Wagner, 1989) discussed in Chapter 4.3 and Chapter 4.4, we use computational models of weakly coupled phase oscillators (reciprocal and unidirectional) to study the interaction of the nose and breathing oscillators.

Figure 41 shows one solution to the reciprocal coupling model with a 78.4 msec propagation time delay, and the intrinsic frequency of the nose oscillator is assumed to be 9.5 Hz ($\omega_N = 19\pi$ radian/s). The intrinsic frequency of the breathing oscillator is 20.4π radian/s (10.2 Hz) during foraging and 16π radian/s (8 Hz) during rearing. The coupling strength of the

interaction is 3.22π radian/s (1.61 Hz) during foraging and 3π radian/s (1.5 Hz) during rearing. With these parameters, the two oscillators can be phase-locked at 11 Hz with a phase difference of -0.107π radians (nose oscillator with respect to breathing oscillator) and be phase-locked at 8 Hz with a phase difference of -0.755π radians during rearing, resulting in a phase shift of 0.648π radians between the two states (Figure 41). The solutions are stable in both states (the stability analysis is discussed in Chapter 4.3).
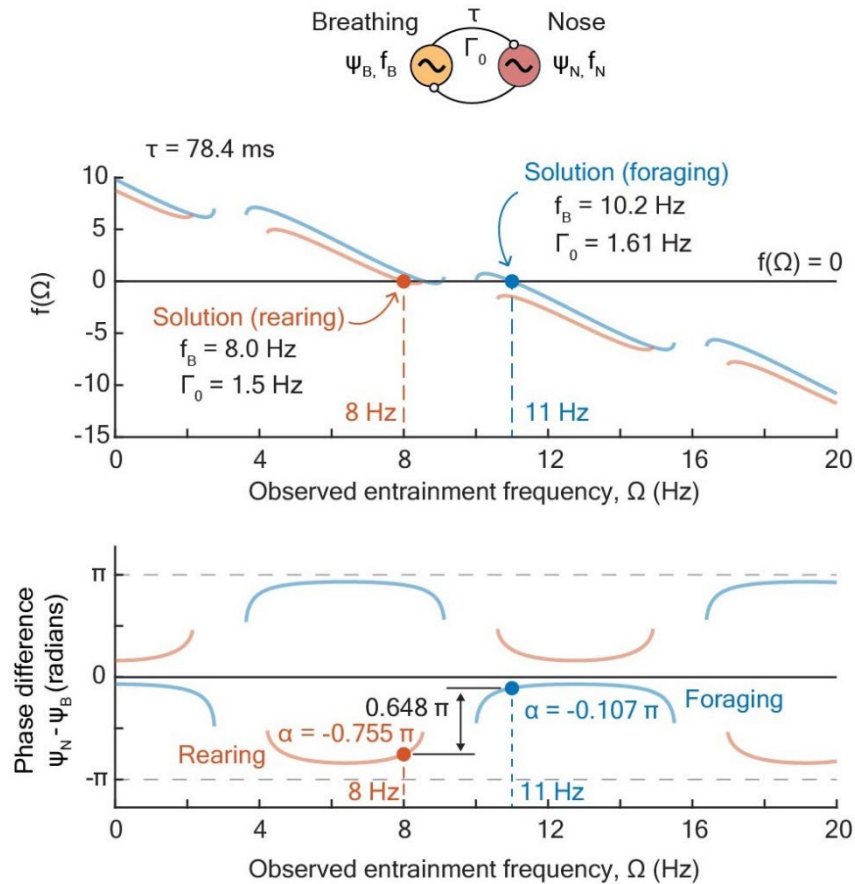
Figure 41: Solution of the reciprocal coupling model for nose twitching. **(Top)** The functional f(Ω) (Eq. 7 in Chapter 4.3) in the foraging (blue) and rearing (red) states. **(Bottom)** The phase difference of the nose oscillator with respect to the breathing oscillator. The phase shift between the two states is 0.648π radians.

By assuming that the intrinsic frequency of the nose oscillator is fixed at 19π radian/s (9.5 Hz), one of the solutions to the unidirectional coupling model is depicted in Figure 42, with 4π radian/s (2.0 Hz) coupling strength and 18 msec time delay. We can generate a phase difference of -0.666π radians in the nose oscillator during the foraging state (driven by 11 Hz sniffing) and a phase delay of -0.018π radians in the rearing state (driven by 8 Hz sniffing). The resultant phase shift is 0.648π radians. The phase-locking is stable in both states (see Chapter 4.4). Figure 42 also shows the range of feasible propagation time delays as a function of the coupling strength. The minimal time delay is 1.7 msec, with the coupling strength of 3.56π radian/s (1.78 Hz).
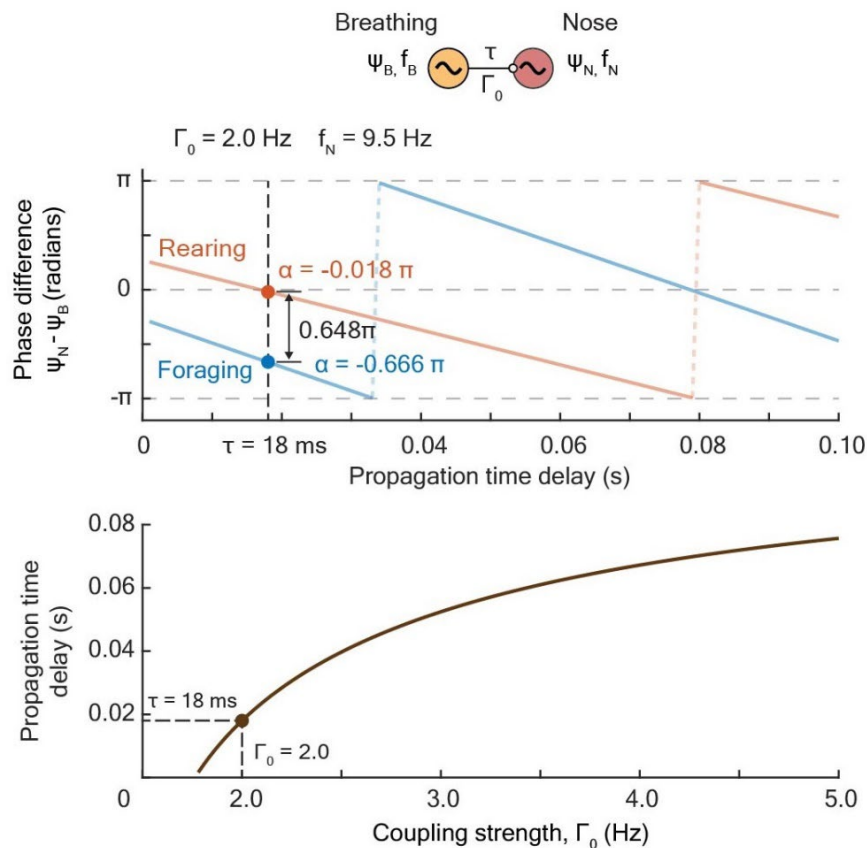
Figure 42: Solution of the unidirectional model for nose twitching. **(Top)** The phase difference between the two oscillators, as a function of the propagation time delay. The solution that gives a phase shift of 0.648π is labeled. **(Bottom)** Solutions of the propagation time delay yielding a phase shift of 0.648π, as a function of the coupling strength.

5.3 Coordination between orofacial motor plants

The functional role of the nose muscle DN is well studied, where unilateral activation draws the nose to the ipsilateral side and upward, and bilateral co-activation draws the nose vertically upward (Deschênes et al., 2015; Kurnikova et al., 2017). To understand the functional contexts of the nose in the foraging and rearing states, we made raster plots of the EMG peaks in the right DN with respect to the peaks in the left DN (Figure 43). We find that in the foraging state, there are more events where only one side of DN is activated (marked by the asterisks in Figure 43) compared to the rearing state (n = 3). It suggests that the rat engages in richer lateral (horizontal) movements of the nose during foraging, possibly for odor localization (Kikuta et al., 2010). The coherence analysis of the left and right DN shows that bilateral co-activation is common in both foraging and rearing states (Figure 44).

Coherence of DN with the ipsilateral neck muscle clavotrapezius (CT) shows that nose-twitching and head scans are phase-locked (Figure 44, n = 3). We normalize bilateral VI and DN EMG envelopes to have zero 50th percentile and unitary difference between the 10th and 90th percentiles. We average the normalized EMG envelopes over clockwise and counterclockwise head scanning peaks (Figure 45). We find that VI and DN are activated during the early phase of head scanning before the head reaches the maximal speed (n = 3 for each muscle). For both VI and DN, the muscle has a greater activity when the head scan is ipsilateral (Figure 45). It suggests that the initiation of head scanning is accompanied by asymmetric whisking and ipsilateral nose-twitching.
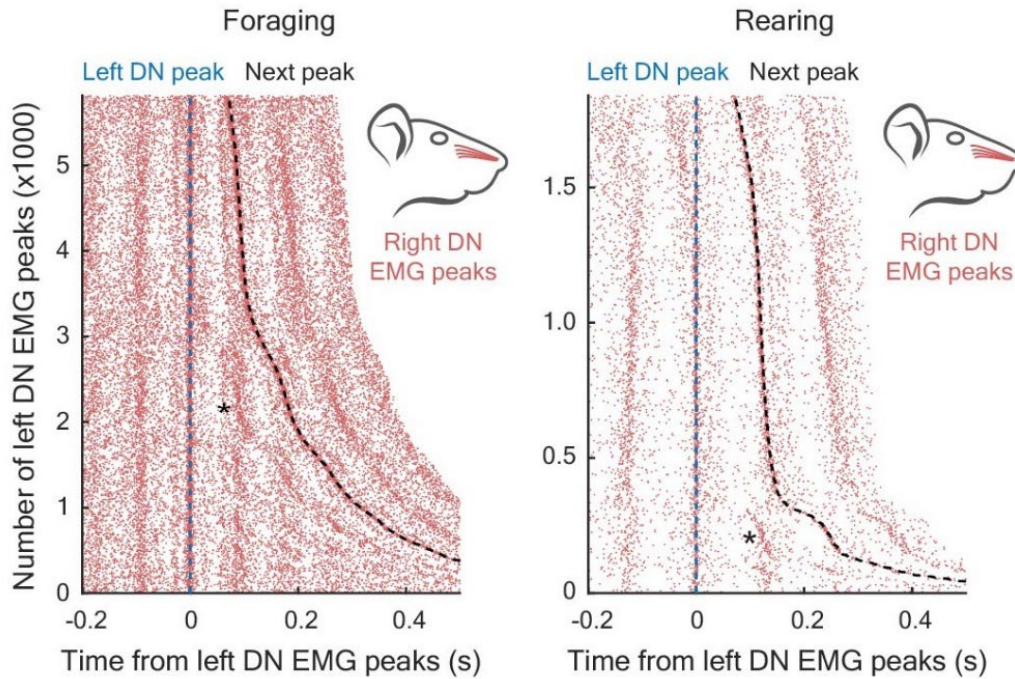
Figure 43: Raster plots of the right DN EMG peaks with respect to the left DN EMG peaks.
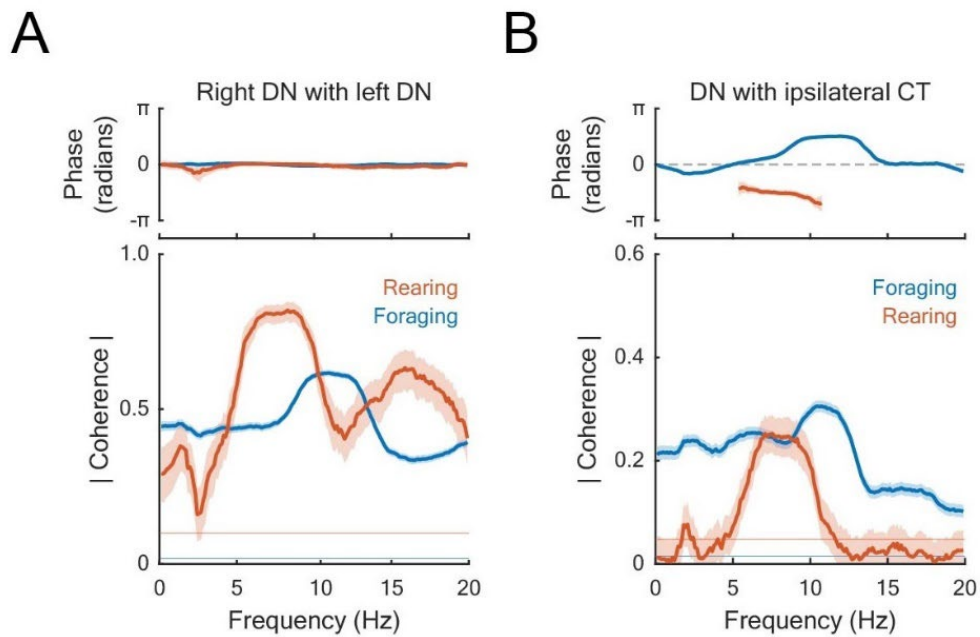
Figure 44: **(A)** Coherence of the right DN with the left DN EMG envelopes. Data from 3 animals. **(B)** Coherence of the left DN with the left CT EMG envelopes. Data from 3 animals. For both plots, the Jackknife errors are shown. The horizontal lines indicate the 95% confidence levels.
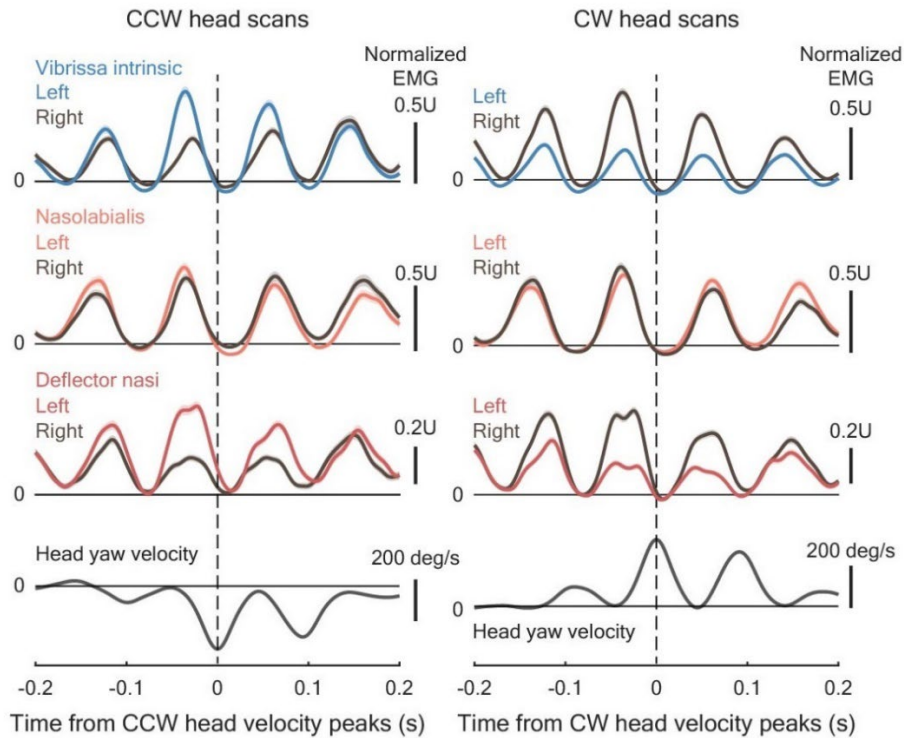
Figure 45: Cross-correlation of the normalized EMG envelopes of VI, NL, and DN with respect to the counterclockwise (left) and clockwise (right) peaks in the head yaw velocity. The head yaw velocity recorded along with the example VI and DN data is also shown (bottom).

5.4 Vibrissal touch during foraging

The observation that the activity is prolonged in VI (n = 3) and advanced in NL (n = 3) is reminiscent of the "touch-induced pump" described by Deutsch et al. (Deutsch et al., 2012; Bellavance et al., 2017). Upon the vibrissal touch, VI motoneurons are transiently inhibited and followed by transient excitation by the reflex loop via the spinal trigeminal nucleus oralis (SpVO) neurons (Bellavance et al., 2017). The advancing activity of NL (Figure 39) is also reminiscent of the touch reflex loop via the spinal trigeminal nucleus rostral interpolaris (SpVIr) neurons that transiently excite NL motoneurons (Bellavance et al., 2017). We hypothesize that during the foraging state, the rat frequently makes vibrissal touches with the floor for tactile information. We

plot the EMG envelopes of VI and NL as a function of the pitch angle of the head in Figure 46. We find that the prolongation of VI activity and the advancement of NL activity is evident when the pitch angle is negative. The effects diminish when the head pitch angle is positive, probably because it becomes harder to make vibrissal contacts to the floor when the head is raised up (touch with the arena wall is still possible). Interestingly, the EMG envelope of DN also shows a varying pattern along the axis of the head pitch angle (Figure 46, n = 7). It suggests that the motor control of the nose might also be modulated by the touch or olfactory response by transient excitation of the motoneurons.

Figure 46: Average EMG envelopes of VI, NL, and DN with respect to the inspiration onsets, as a function of the head pitch angle. Data from individual animals. Standard errors are shown. The anatomical illustration of VI is adapted from Hill et al., 2008.

Acknowledgements

Chapter 6. Discussion

6.1 Neck muscles recruited by distinct respiratory phases

We delineate the coordination of head scanning with breathing in rats performing naturalistic foraging behaviors. Our work shows that neck muscles are coordinated by different phases in breathing. During foraging, muscles clavotrapezius (CT), splenius (SP), and biventer cervicis (BC) are activated during inspiration, while muscles sternomastoid (SM) and cleidomastoid (CM) are recruited during expiration (Chapter 4.1). With the muscle synergies, the rat makes inward head scanning during inspiration and outward head scanning during expiration (Chapter 3.3). The results support two aspects of the breathing primacy hypothesis (Chapter 1.2).

First, phase-locking between the neck motor actions and sniffing suggests that the breathing oscillator is involved in the hierarchical control of the head motion. From the point of view of motor output, since numerous neck muscles can contribute to the movements of the head (Bekele, 1983), it may be more efficient to send out the motor commands to these motoneuron pools by binding them with the breathing rhythm to ensure precise timing. From the point of view of sensory input, many orofacial motor plants are moved by the head. Using breathing as a reference clock to scan the head can guarantee that multimodal sensory inputs, such as olfactory (Smear et al., 2011) and tactile signals (Moore et al., 2013), can be processed at a proper temporal and spatial resolution (Moore et al., 2013; Kleinfeld et al., 2014; Moore et al., 2014).

Second, the observations that (1) expiratory head scanning has a faster (on average) speed than inspiratory head scanning and (2) the outward head scanning in the egocentric coordinates occurs during expiration (Chapter 3.3) are both consistent with the notion that in rodents the expiratory phase is mainly used for relocating the motor plants for the subsequent sampling "snapshot" (Uchida and Mainen, 2003; Moore et al., 2013; Kurnikova et al., 2017). The rat also

mainly uses the expiratory phase to relocate the head vertically in the head-bobbing behavior (Kurnikova et al., 2017). Therefore, the motor strategy of head movement is similar on both the vertical and horizontal axes.

What neural configuration is lying behind these observations? Currently, we don't have enough information to answer this because of the lack of complete understanding of the neural circuitry for the neck and its connection with the breathing oscillators. Although the distributions of the motoneuron pools of the five neck muscles (SM, CM, CT, SP, and BC) in this work were well studied (Brichta et al., 1987; Callister et al., 1987), the mapping of their premotor neurons in rodents has not been fully investigated. The reticular formation is a prospective region that may contain neck premotor neurons in rodents. Spinal cord-projecting neurons in the medial reticular formation are crucial in head orienting in rats, and they receive inputs from the contralateral superior colliculus (Dean et al., 1988; Dean et al., 1989). Optogenetic stimulation of spinal cord-projecting neurons in the medial rostral medulla induces ipsilateral head turning in mice (Ruder et al., 2021). Retrograde tracing with Cholera toxin subunit B from sternomastoid (SM) reveals labeled neurons in the reticular formation (Hayakawa et al., 2002). These results suggest that the premotor circuity for head-turning might reside in the reticular formation. In addition to the reticular formation, coordination between neck motor neurons may involve the spinal interneurons in the propriospinal networks (Sunshine et al., 2020). Intraspinal microstimulation from C2 to T1 can elicit sternomastoid activity in rats (Sunshine et al., 2018). Unraveling the promotor circuitries of the neck motoneurons will reveal the sources and pathways of the respiratory drives that entrain the head movement. Also, it was reported that no significant direct projections from the preBötC to the spinal cord were observed (Tan et al., 2010). Therefore, the pathway of the respiratory drive might involve the neck premotor circuitries, the relays of the respiratory oscillators (Dobbins and

Feldman, 1994; Tan et al., 2010), or the high cervical respiratory group in the cervical spinal cord (Oku et al., 2008; Kobayashi et al., 2010). In the future, retrograde labeling of the premotor neurons of the neck muscles can help us understand the pathways of the respiratory drives.

Lastly, the dorsal neck muscle splenius, which shows inspiratory activity in head scanning (Chapter 4.1), is also activated during expiration in the head-bobbing behavior (Kurnikova et al., 2017). Motor commands of the horizontal and vertical head control are found to descend via distinct pathways in cats (Isa and Naito, 1994; Isa and Naito, 1995; Isa and Sasaki, 2002). In the future, it will be interesting to ask whether the motor commands for head movements in these two orthogonal directions take different pathways via the breathing oscillators in rodents.

6.2 Phase shift between behavioral states

We find that as the rat changes its behavioral contexts from foraging to rearing, muscles sternomastoid (SM) and cleidomastoid (CM) shift their phase relationship with sniffing from expiratory to inspiratory activity, while muscles splenius (SP) and biventer cervicis (BC) shift their phase relationship with sniffing from inspiratory to expiratory activity (Chapter 4.1, Figure 47). The phase shift is accompanied by a frequency shift in the entrainment rhythm with breathing (Chapter 3.2). We model these observations by computational models of weakly coupled oscillators (Schuster and Wagner, 1989) formed by the breathing and neck oscillators (Chapters 4.3-4.4). We show that with a propagation time delay (79.9 msec) and a constant intrinsic frequency (assumed to be at 9.5 Hz) in the neck oscillator, a reciprocal model can generate a phase shift of ~0.8π radians when the breathing oscillator takes on different intrinsic frequencies (with a slight change in the coupling strength) in the two behavioral states. In the meantime, the neck and breathing oscillators can be phase-locked at 8 Hz during rearing and 11 Hz during foraging

(Chapter 4.3). In the unidirectional model, a time delay of 27 msec can have the neck oscillator be driven at 8 Hz during rearing and 11 Hz during foraging by the breathing oscillator, as the phase difference shifts by π radians between the two behavioral states (Chapter 4.4). Both models suggest that by driving the sniffing rate at different frequencies, the rat can entrain the neck muscles at different phases in the sniff cycle to fulfill specific behavioral needs or functional goals with fixed connectivity in the brainstem circuitry (Figure 48). This process probably also involves neuromodulations such as the degree of hunger/satiety (Lever et al., 2006; Marder, 2012). The question that which (reciprocal or unidirectional) model is closer to the biological world relies on future studies on neck premotor connectomics.
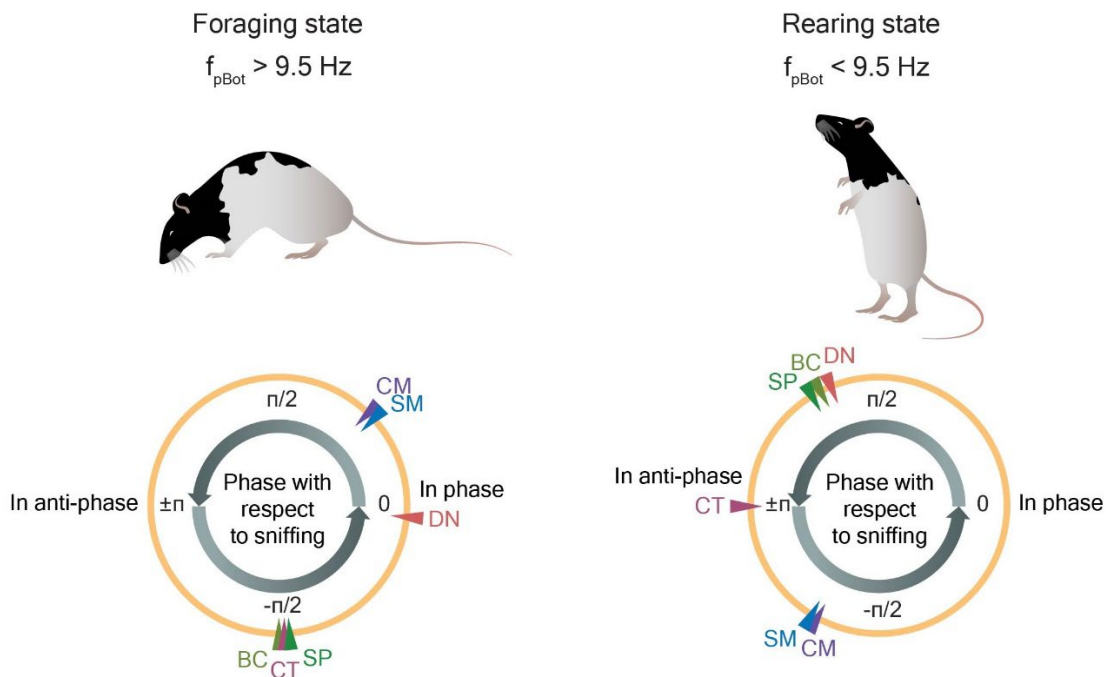
Figure 47: Illustration of the phase relationship with sniffing in the neck (SM, CM, CT, SP, and BC) and nose (DN) muscles during foraging versus rearing.
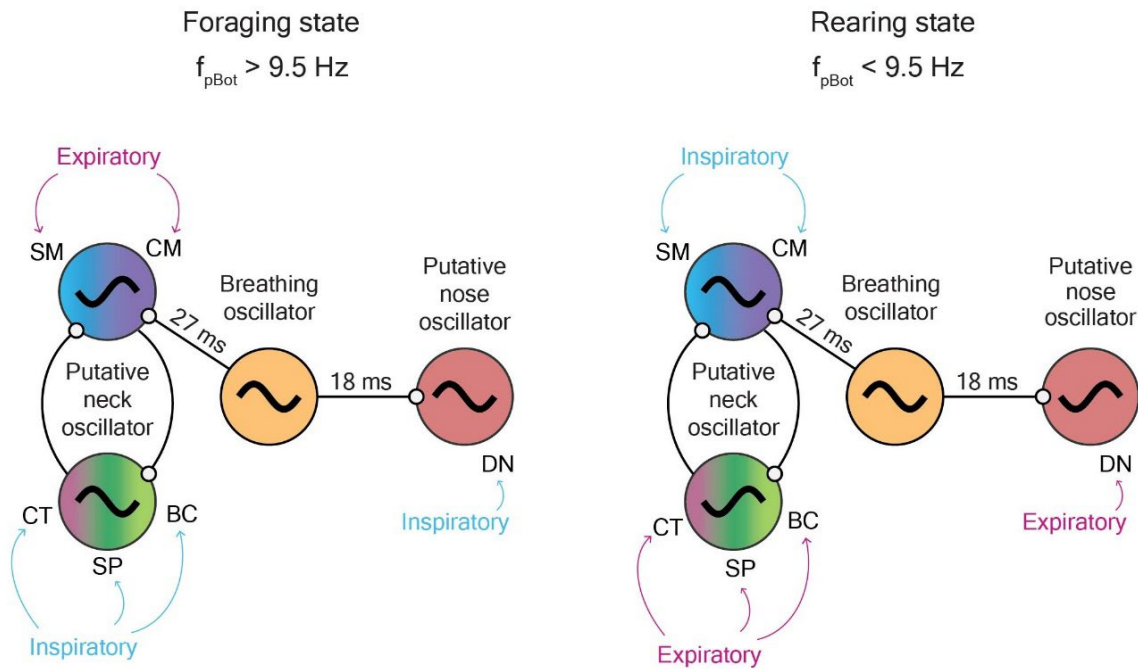
Figure 48: Depiction of the interaction between breathing and head (or nose) movement using the model of unidirectionally coupled oscillators. The breathing entrains the neck (or nose) oscillator by driving the sniffing frequency (f_{pBot}) at different rates. Feasible time delays for the interactions are shown.

We end by noting that the phenomenon where the phase relationships change with various frequencies (or speeds) is also observed in animal locomotion formed by different gaits, such as walking, trotting, and galloping (von Holst, 1939/1973; Maes and Abourachid, 2013; Lemieux et al., 2016; Boije and Kullander, 2018). Models of coupled phase oscillators have been used to study the phenomenon (reviewed in Holmes et al., 2006). The spinal segments or the limbs are modeled as oscillators, and transitions between different modes of swimming in fish (Kopell and Ermentrout, 1986; Kopell, 1988), or different gaits in tetrapods (Buchli and Ijspeert, 2004), insects (Ghigliazza and Holmes, 2004), and myriapods (Golubitsky et al., 1998) can be achieved by varying the coupling strengths among the oscillators. Our work suggests that similar computational models might also be used to study the switching between exploratory behaviors in the rat.

6.3 Motor control of head with nose and vibrissae

In this work, we delineate the coordination of the nose and vibrissae with breathing in the foraging and rearing states. The vibrissa intrinsic muscle (VI), nasolabialis (NL), and deflector nasi (DN) all show different activation patterns between the two states (Chapter 5.1).

As the rat switches from foraging to rearing, deflector nasi shifts its respiratory activity from the inspiratory phase to the expiratory phase by $\sim 0.648\pi$ radians (Figure 40; Figure 47). We show that a computational model of weakly coupled oscillators, with either reciprocal or unidirectional connection, can yield this phase shift (Chapter 5.2). Like the motor control of the head movement, a frequency shift in the sniffing rate might be a means the rat uses to recruit deflector nasi at different phases in the sniffing cycle (Figure 48). Premotor neurons of deflector nasi have been identified in the reticular formation, and some of them receive the projection from preBötC (Kurnikova et al., 2019). These findings established the connection from the breathing oscillator to the nose oscillator. Whether the projection from the nose oscillator to the breathing oscillator exists awaits further investigation.

Our EMG data from the vibrissae muscles (VI and NL) suggest the participation of active touch reflex loops via SpVIr and SpVO (Bellavance et al., 2017) in the foraging process (Chapter 5.4). The latency time of the touch reflex loop for VI motoneurons was estimated to be 11 to 13 milliseconds (Mitchinson et al., 2007; Bellavance et al., 2017). This timescale is consistent with the prolongation in VI activity we observe in the EMG data (Figure 38). The correlated movement of vibrissae with breathing (Figure 38, Figure 39) suggests that there might exist a "preferred respiratory phase for touch" in the rat nervous system. By precise coordination with the movement of the head and breathing, the vibrissae can touch the floor during protraction at a specific inspiratory phase in the sniffing cycle. Neurons in SpVO were found to send projections to the

cervical spinal cord (Devoize et al., 2010), which might serve as the substrate for vibrissae-neck coordination. In head-fixed mice, the phase coding in S1 during surface whisking is preferred during protraction (Isett and Feldman, 2020). The surface coding might also be preferred at protraction during inspiration in foraging rats, with coordinated movements of the vibrissae and the head to ensure proper timing of the contacts (Towal and Hartmann, 2006; Grant et al., 2012; Ranade et al., 2013; Sherman et al., 2013; Hobbs et al., 2015; Tsur et al., 2019).

Lastly, in addition to the vibrissae muscles, the activation of the nose muscle deflector nasi also shows a dependency on the head pitch angle (Figure 46). It suggests that tactile or olfactory signals might be the factors that modulate the motor control of the nose. Past studies have shown that ablating the glutamatergic premotor neurons of DN in the retrofacial area affected nose movements in response to odor (Kurnikova et al., 2019). Whether or not the advanced activation of DN reflects the odor response or any unidentified touch reflex loop needs further investigation.

Acknowledgements

REFERENCES

Anderson, T. M., Garcia III, A. J., Baertsch, N. A., Pollak, J., Bloom, J. C., Wei, A. D., Rai, K. G., & Ramirez, J. M. (2016). A novel excitatory network for the control of breathing. Nature, 536(7614), 76–80.

Bellavance, M. A., Takatoh, J., Lu, J., Demers, M., Kleinfeld, D., Wang, F., & Deschênes, M. (2017). Parallel inhibitory and excitatory trigemino-facial feedback circuitry for reflexive vibrissa movement. Neuron, 95(3), 673–682.

Bekele, A. (1983). The comparative functional morphology of some head muscles of the rodents Tachyoryctes splendens and Rattus rattus. II. Cervical muscles. Mammalia, 47(4), 549-572.

Benjamini, Y., Fonio, E., Galili, T., Havkin, G. Z., & Golani, I. (2011). Quantifying the buildup in extent and complexity of free exploration in mice. Proceedings of the National Academy of Sciences, 108(supplement_3), 15580-15587.

Berg, R. W., & Kleinfeld, D. (2003). Rhythmic whisking by rat: retraction as well as protraction of the vibrissae is under active muscular control. Journal of Neurophysiology, 89(1), 104-117.

Boije, H., & Kullander, K. (2018). Origin and circuitry of spinal locomotor interneurons generating different speeds. Current Opinion in Neurobiology, 53, 16-21.

Brichta, A. M., Callister, R. J., & Peterson, E. H. (1987). Quantitative analysis of cervical musculature in rats: histochemical composition and motor pool organization. I. Muscles of the spinal accessory complex. Journal of Comparative Neurology, 255(3), 351–368.

Buchli, J., & Ijspeert, A. J. (2004). Distributed central pattern generator model for robotics application based on phase sensitivity analysis. In A. J. Ijspeert, M. Murata & N. Wakamiya (Eds.), International workshop on biologically inspired approaches to advanced information technology (pp. 333-349). Springer, Berlin, Heidelberg.

Callister, R. J., Brichta, A. M., & Peterson, E. H. (1987). Quantitative analysis of cervical musculature in rats: histochemical composition and motor pool organization. II. Deep dorsal muscles. Journal of Comparative Neurology, 255(3), 369–385.

Chandler, S. H., & Tal, M. (1986). The effects of brain stem transections on the neuronal networks responsible for rhythmical jaw muscle activity in the guinea pig. Journal of Neuroscience, 6(6), 1831-1842.

Chen, Z., Travers, S. P., & Travers, J. B. (2001). Muscimol infusions in the brain stem reticular formation reversibly block ingestion in the awake rat. American Journal of Physiology-Regulatory, Integrative and Comparative Physiology, 280(4), R1085-R1094.

Cohen, A. H., Holmes, P. J., & Rand, R. H. (1982). The nature of the coupling between segmental oscillators of the lamprey spinal generator for locomotion: A mathematical model. Journal of Mathematical Biology, 13(3), 345-369.

Dean, P., Redgrave, P., & Mitchell, I. J. (1988). Organisation of efferent projections from superior colliculus to brainstem in rat: evidence for functional output channels. Progress in Brain Research, 75, 27–36.

Dean, P., Redgrave, P., & Westby, G. W. (1989). Event or emergency? Two response systems in the mammalian superior colliculus. Trends in Neurosciences, 12(4), 137–147.

Del Negro, C. A., Funk, G. D., & Feldman, J. L. (2018). Breathing matters. Nature Reviews Neuroscience, 19(6), 351–367.

Delaney, K. R., Gelperin, A., Fee, M. S., Flores, J. A., Gervais, R., Tank, D. W., & Kleinfeld, D. (1994). Waves and stimulus-modulated dynamics in an oscillating olfactory network. Proceedings of the National Academy of Sciences, 91(2), 669-673.

Dempsey, B., Sungeelee, S., Bokiniec, P., Chettouh, Z., Diem, S., Autran, S., Harrell, E. R., Poulet, J. F. A., Birchmeier, C., Carey, H., Genovesio, A., McMullan, S., Goridis, C., Fortin, G., & Brunet, J. F. (2021). A medullary centre for lapping in mice. Nature Communications, 12(1), 1-12.

Deschênes, M., Haidarliu, S., Demers, M., Moore, J., Kleinfeld, D., & Ahissar, E. (2015). Muscles involved in naris dilation and nose motion in rat. The Anatomical Record, 298(3), 546–553.

Deschênes, M., Takatoh, J., Kurnikova, A., Moore, J. D., Demers, M., Elbaz, M., Furuta, T., Wang, F., & Kleinfeld, D. (2016). Inhibition, not excitation, drives rhythmic whisking. Neuron, 90(2), 374–387.

Deutsch, D., Pietr, M., Knutsen, P. M., Ahissar, E., & Schneidman, E. (2012). Fast feedback in active sensing: touch-induced changes to whisker-object interaction. PLoS ONE, 7(9), e44272.

Devoize, L., Doméjean, S., Melin, C., Raboisson, P., Artola, A., & Dallel, R. (2010). Organization of projections from the spinal trigeminal subnucleus oralis to the spinal cord in the rat: a neuroanatomical substrate for reciprocal orofacial-cervical interactions. Brain Research, 1343, 75–82.

Dobbins, E. G., & Feldman, J. L. (1994). Brainstem network controlling descending drive to phrenic motoneurons in rat. Journal of Comparative Neurology, 347(1), 64–86.

Ermentrout, G. B., & Kleinfeld, D. (2001). Traveling electrical waves in cortex: insights from phase dynamics and speculation on a computational role. Neuron, 29(1), 33-44.

Findley, T. M., Wyrick, D. G., Cramer, J. L., Brown, M. A., Holcomb, B., Attey, R., Yeh, D., Monasevitch, E., Nouboussi, N., Cullen, I., Songco, J. O., King, J. F., Ahmadian, Y., & Smear, M. C. (2021). Sniff-synchronized, gradient-guided olfactory search by freely moving mice. eLife, 10, e58523.

Fonio, E., Benjamini, Y., & Golani, I. (2009). Freedom of movement and the stability of its unfolding in free exploration of mice. Proceedings of the National Academy of Sciences, 106(50), 21335-21340.

Gal, O. (2022). fit_ellipse. https://www.mathworks.com/matlabcentral/fileexchange/3215-fit_ellipse, MATLAB Central File Exchange.

Gharbawie, O. A., Whishaw, P. A., & Whishaw, I. Q. (2004). The topography of three-dimensional exploration: a new quantification of vertical and horizontal exploration, postural support, and exploratory bouts in the cylinder test. Behavioural Brain Research, 151(1-2), 125-135.

Ghigliazza, R. M., & Holmes, P. (2004). A minimal model of a central pattern generator and motoneurons for insect locomotion. SIAM Journal on Applied Dynamical Systems, 3(4), 671-700.

Golani, I., Wolgin, D. L., & Teitelbaum, P. (1979). A proposed natural geometry of recovery from akinesia in the lateral hypothalamic rat. Brain Research, 164(1-2), 237-267.

Golubitsky, M., Stewart, I., Buono, P. L., & Collins, J. J. (1998). A modular network for legged locomotion. Physica D: Nonlinear Phenomena, 115(1-2), 56-72.

Grant, R. A., Sperber, A. L., & Prescott, T. J. (2012). The role of orienting in vibrissal touch sensing. Frontiers in Behavioral Neuroscience, 6, 39.

Guyenet, P. G., Bayliss, D. A., Stornetta, R. L., Fortuna, M. G., Abbott, S. B., & DePuy, S. D. (2009). Retrotrapezoid nucleus, respiratory chemosensitivity and breathing automaticity. Respiratory Physiology & Neurobiology, 168(1-2), 59-68.

Hargreaves, E. L., & Cain, D. P. (1992). Hyperactivity, hyper-reactivity, and sensorimotor deficits induced by low doses of the N-methyl-D-aspartate non-competitive channel blocker MK801. Behavioural Brain Research, 47(1), 23-33.

Hayakawa, T., Takanaga, A., Tanaka, K., Maeda, S., & Seki, M. (2002). Organization and distribution of the upper and lower esophageal motoneurons in the medulla and the spinal cord of the rat. Okajimas Folia Anatomica Japonica, 78(6), 263-279.

He, K., Zhang, X., Ren, S., & Sun, J. (2016). Deep residual learning for image recognition. In Proceedings of the IEEE conference on computer vision and pattern recognition (pp. 770-778).

Hill, D. N., Bermejo, R., Zeigler, H. P., & Kleinfeld, D. (2008). Biomechanics of the vibrissa motor plant in rat: rhythmic whisking consists of triphasic neuromuscular activity. Journal of Neuroscience, 28(13), 3438-3455.

Hobbs, J. A., Towal, R. B., & Hartmann, M. J. (2015). Probability distributions of whisker-surface contact: quantifying elements of the rat vibrissotactile natural scene. The Journal of Experimental Biology, 218(16), 2551–2562.

Holmes, P., Full, R. J., Koditschek, D., & Guckenheimer, J. (2006). The dynamics of legged locomotion: Models, analyses, and challenges. SIAM Review, 48(2), 207-304.

von Holst, E. (1939/1973). Relative coordination as a phenomenon and as a method of analysis of central nervous functions. In R. Martin (Ed.), The behavioural physiology of animals and man: the collected papers of Erich von Holst, volume 1 (pp. 33-135). University of Miami Press, Coral Gables, Florida.

Huckstepp, R. T., Cardoza, K. P., Henderson, L. E., & Feldman, J. L. (2015). Role of parafacial nuclei in control of breathing in adult rats. Journal of Neuroscience, 35(3), 1052–1067.

Insafutdinov, E., Pishchulin, L., Andres, B., Andriluka, M., & Schiele, B. (2016). Deepercut: A deeper, stronger, and faster multi-person pose estimation model. In European conference on computer vision (pp. 34-50). Springer, Cham.

Isa, T., & Naito, K. (1994). Activity of neurons in Forel's field H during orienting head movements in alert head-free cats. Experimental Brain Research, 100(2), 187-199.

Isa, T., & Naito, K. (1995). Activity of neurons in the medial pontomedullary reticular formation during orienting movements in alert head-free cats. Journal of Neurophysiology, 74(1), 73-95.

Isa, T., & Sasaki, S. (2002). Brainstem control of head movements during orienting; organization of the premotor circuits. Progress in Neurobiology, 66(4), 205–241.

Isett, B. R., & Feldman, D. E. (2020). Cortical coding of whisking phase during surface whisking. Current Biology, 30(16), 3065–3074.

Janczewski, W. A., & Feldman, J. L. (2006). Distinct rhythm generators for inspiration and expiration in the juvenile rat. The Journal of Physiology, 570(2), 407-420.

Kepecs, A., Uchida, N., & Mainen, Z. F. (2007). Rapid and precise control of sniffing during olfactory discrimination in rats. Journal of Neurophysiology, 98(1), 205-213.

Kikuta, S., Sato, K., Kashiwadani, H., Tsunoda, K., Yamasoba, T., & Mori, K. (2010). Neurons in the anterior olfactory nucleus pars externa detect right or left localization of odor sources. Proceedings of the National Academy of Sciences, 107(27), 12363-12368.

Kleinfeld, D., & Mehta, S. B. (2006). Spectral mixing in nervous systems: experimental evidence and biologically plausible circuits. Progress of Theoretical Physics Supplement, 161, 86-98.

Kleinfeld, D., & Mitra, P. P. (2014). Spectral methods for functional brain imaging. Cold Spring Harbor Protocols, 2014(3), 248–262.

Kleinfeld, D., Deschênes, M., Wang, F., & Moore, J. D. (2014). More than a rhythm of life: breathing as a binder of orofacial sensation. Nature Neuroscience, 17(5), 647–651.

Kobayashi, S., Fujito, Y., Matsuyama, K., & Aoki, M. (2010). Spontaneous respiratory rhythm generation in in vitro upper cervical slice preparations of neonatal mice. The Journal of Physiological Sciences, 60(4), 303–307.

Kopell, N., & Ermentrout, G. B. (1986). Symmetry and phaselocking in chains of weakly coupled oscillators. Communications on Pure and Applied Mathematics, 39(5), 623-660.

Kopell, N. (1988). Toward a theory of modelling central pattern generators. In A. H. Cohen, S. Rossignol & S. Grillner (Eds.), Neural control of rhythmic movements in vertebrates (pp. 369-413). Wiley.

Kuramoto, Y. (1984). Chemical oscillations, waves, and turbulence. Springer, Berlin, Heidelberg.

Kurnikova, A., Moore, J. D., Liao, S.-M., Deschênes, M., & Kleinfeld, D. (2017). Coordination of orofacial motor actions into exploratory behavior by rat. Current Biology, 27(5), 688–696.

Kurnikova, A., Deschênes, M., & Kleinfeld, D. (2019). Functional brain stem circuits for control of nose motion. Journal of Neurophysiology, 121(1), 205–217.

Lemieux, M., Josset, N., Roussel, M., Couraud, S., & Bretzner, F. (2016). Speed-dependent modulation of the locomotor behavior in adult mice reveals attractor and transitional gaits. Frontiers in Neuroscience, 10, 42.

Lever, C., Burton, S., & O'Keefe, J. (2006). Rearing on hind legs, environmental novelty, and the hippocampal formation. Reviews in the Neurosciences, 17(1-2), 111-133.

Loeb, G. E., & Gans, C. (1986). Electromyography for experimentalists. University of Chicago press.

Maes, L., & Abourachid, A. (2013). Gait transitions and modular organization of mammal locomotion. Journal of Experimental Biology, 216(12), 2257-2265.

Marder E. (2012). Neuromodulation of neuronal circuits: back to the future. Neuron, 76(1), 1–11.

Mathis, A., Mamidanna, P., Cury, K. M., Abe, T., Murthy, V. N., Mathis, M. W., & Bethge, M. (2018). DeepLabCut: markerless pose estimation of user-defined body parts with deep learning. Nature Neuroscience, 21(9), 1281-1289.

McElvain, L. E., Friedman, B., Karten, H. J., Svoboda, K., Wang, F., Deschênes, M., & Kleinfeld, D. (2018). Circuits in the rodent brainstem that control whisking in concert with other orofacial motor actions. Neuroscience, 368, 152-170.

Mitchinson, B., Martin, C. J., Grant, R. A., & Prescott, T. J. (2007). Feedback control in active sensing: rat exploratory whisking is modulated by environmental contact. Proceedings of the Royal Society B: Biological Sciences, 274(1613), 1035-1041.

Mitra, P. P., & Bokil, H. (2008). Observed brain dynamics. Oxford University Press, New York.

Moore, J. D., Deschênes, M., Furuta, T., Huber, D., Smear, M. C., Demers, M., & Kleinfeld, D. (2013). Hierarchy of orofacial rhythms revealed through whisking and breathing. Nature, 497(7448), 205–210.

Moore, J. D., Kleinfeld, D., & Wang, F. (2014). How the brainstem controls orofacial behaviors comprised of rhythmic actions. Trends in Neurosciences, 37(7), 370–380.

Nakamura, Y., & Katakura, N. (1995). Generation of masticatory rhythm in the brainstem. Neuroscience Research, 23(1), 1–19.

Nath, T., Mathis, A., Chen, A. C., Patel, A., Bethge, M., & Mathis, M. W. (2019). Using DeepLabCut for 3D markerless pose estimation across species and behaviors. Nature Protocols, 14(7), 2152-2176.

Nozaki, S., Iriki, A., & Nakamura, Y. (1986). Localization of central rhythm generator involved in cortically induced rhythmical masticatory jaw-opening movement in the guinea pig. Journal of Neurophysiology, 55(4), 806-825.

Oku, Y., Okabe, A., Hayakawa, T., & Okada, Y. (2008). Respiratory neuron group in the high cervical spinal cord discovered by optical imaging. Neuroreport, 19(17), 1739–1743.

Pearce, R. A., Stornetta, R. L., & Guyenet, P. G. (1989). Retrotrapezoid nucleus in the rat. Neuroscience Letters, 101(2), 138-142.

Ramirez, J. M., & Baertsch, N. A. (2018). The dynamic basis of respiratory rhythm generation: one breath at a time. Annual Review of Neuroscience, 41, 475–499.

Ranade, S., Hangya, B., & Kepecs, A. (2013). Multiple modes of phase locking between sniffing and whisking during active exploration. Journal of Neuroscience, 33(19), 8250–8256.

Roelfsema, P. R., Engel, A. K., König, P., & Singer, W. (1997). Visuomotor integration is associated with zero time-lag synchronization among cortical areas. Nature, 385(6612), 157-161.

Ruder, L., Schina, R., Kanodia, H., Valencia-Garcia, S., Pivetta, C., & Arber, S. (2021). A functional map for diverse forelimb actions within brainstem circuitry. Nature, 590(7846), 445–450.

Schuster, H. G., & Wagner, P. (1989). Mutual entrainment of two limit cycle oscillators with time delayed coupling. Progress of Theoretical Physics, 81(5), 939–945.

Sherman, D., Oram, T., Deutsch, D., Gordon, G., Ahissar, E., & Harel, D. (2013). Tactile modulation of whisking via the brainstem loop: statechart modeling and experimental validation. PLoS ONE, 8(11), e79831.

Shusterman, R., Smear, M. C., Koulakov, A. A., & Rinberg, D. (2011). Precise olfactory responses tile the sniff cycle. Nature Neuroscience, 14(8), 1039–1044.

Smear, M., Shusterman, R., O'Connor, R., Bozza, T., & Rinberg, D. (2011). Perception of sniff phase in mouse olfaction. Nature, 479(7373), 397–400.

Smith, J. C., Ellenberger, H. H., Ballanyi, K., Richter, D. W., & Feldman, J. L. (1991). Pre-Bötzinger complex: a brainstem region that may generate respiratory rhythm in mammals. Science, 254(5032), 726–729.

Stanek IV, E., Cheng, S., Takatoh, J., Han, B.-X., & Wang, F. (2014). Monosynaptic premotor circuit tracing reveals neural substrates for oro-motor coordination. Elife, 3, e02511.

Sunshine, M. D., Ganji, C. N., Reier, P. J., Fuller, D. D., & Moritz, C. T. (2018). Intraspinal microstimulation for respiratory muscle activation. Experimental Neurology, 302, 93–103.

Sunshine, M. D., Sutor, T. W., Fox, E. J., & Fuller, D. D. (2020). Targeted activation of spinal respiratory neural circuits. Experimental Neurology, 328, 113256.

Takatoh, J., Prevosto, V., Thompson, P. M., Lu, J., Chung, L., Harrahill, A., Li, S., Zhao, S., He, Z., Golomb, D., Kleinfeld, D., & Wang, F. (2022). The whisking oscillator circuit. Nature, in press.

Tan, W., Pagliardini, S., Yang, P., Janczewski, W. A., & Feldman, J. L. (2010). Projections of preBötzinger complex neurons in adult rats. Journal of Comparative Neurology, 518(10), 1862–1878.

Towal, R. B., & Hartmann, M. J. (2006). Right–left asymmetries in the whisking behavior of rats anticipate head movements. Journal of Neuroscience, 26(34), 8838-8846.

Travers, J. B., DiNardo, L. A., & Karimnamazi, H. (1997). Motor and premotor mechanisms of licking. Neuroscience & Biobehavioral Reviews, 21(5), 631–647.

Travers, J. B., DiNardo, L. A., & Karimnamazi, H. (2000). Medullary reticular formation activity during ingestion and rejection in the awake rat. Experimental Brain Research, 130(1), 78-92.

Tsur, O., Khrapunsky, Y., & Azouz, R. (2019). Sensorimotor integration in the whisker somatosensory brain stem trigeminal loop. Journal of Neurophysiology, 122(5), 2061–2075.

Uchida, N., & Mainen, Z. F. (2003). Speed and accuracy of olfactory discrimination in the rat. Nature Neuroscience, 6(11), 1224–1229.

Viswanathan, G. M., Raposo, E. P., Bartumeus, F., Catalan, J., & Da Luz, M. G. E. (2005). Necessary criterion for distinguishing true superdiffusion from correlated random walk processes. Physical Review E, 72(1), 011111.

Viswanathan, G. M., Da Luz, M. G., Raposo, E. P., & Stanley, H. E. (2011). The physics of foraging: an introduction to random searches and biological encounters. Cambridge University Press.

Welker, W. I. (1964) Analysis of sniffing of the albino rat. Behaviour, 22, 223-244.

Wexler, Y., Benjamini, Y., & Golani, I. (2018). Vertical exploration and dimensional modularity in mice. Royal Society Open Science, 5(3), 180069.

Wu, J., Zou, H., Strong, J. A., Yu, J., Zhou, X., Xie, Q., Zhao, G., Jin, M., & Yu, L. (2005). Bimodal effects of MK-801 on locomotion and stereotypy in C57BL/6 mice. Psychopharmacology, 177(3), 256-263.